Oil & Natural Gas Technology

DOE Award No.: DE-FC26-06NT42956

Final Report

Natural and Induced Fracture Diagnostics from 4-D VSP in Low Permeability Gas Reservoirs

Submitted by:
Earth Resources Laboratory
Department of Earth, Atmospheric, and Planetary Sciences
Massachusetts Institute of Technology
Cambridge, MA 02139

Prepared for:
United States Department of Energy
National Energy Technology Laboratory

Office of Fossil Energy

NATURAL AND INDUCED FRACTURE DIAGNOSTICS FROM 4-D VSP IN LOW PERMEABILITY GAS RESERVOIRS

FINAL REPORT

October 1, 2006 – September 30, 2008

by

Mark E. Willis, Daniel R. Burns, and M. Nafi Toksöz

Earth Resources Laboratory
Department of Earth, Atmospheric, and Planetary Sciences
Massachusetts Institute of Technology
Cambridge, MA 02139

January 30, 2009

Prepared for
THE U.S. DEPARTMENT OF ENERGY
AWARD NUMBER DE-FC26-06NT42956

This technical progress report was prepared with the support of the U.S. Department of Energy, under Award No. DE-FC26-06NT42956. However, any opinions, findings, conclusions, or recommendations expressed herein are those of the authors and do not necessarily reflect the views of the DOE.

DISCLAIMER

Abstract

Tight gas sand reservoirs generally contain thick gas-charged intervals that often have low porosity and very low permeability. Natural and induced fractures provide the only means of production. The objective of this work is to locate and characterize natural and induced fractures from analysis of scattered waves recorded on 4-D (time lapse) VSP data in order to optimize well placement and well spacing in these gas reservoirs. Using model data simulating the scattering of seismic energy from hydraulic fractures, we first show that it is possible to characterize the quality of fracturing based upon the amount of scattering. In addition, the picked arrival times of recorded microseismic events provide the velocity moveout for isolating the scattered energy on the 4-D VSP data.

This concept is applied to a field dataset from the Jonah Field in Wyoming to characterize the quality of the induced hydraulic fractures. The time lapse (4D) VSP data from this field are imaged using a migration algorithm that utilizes shot travel time tables derived from the first breaks of the 3D VSPs and receiver travel time tables based on the microseismic arrival times and a regional velocity model. Four azimuthally varying shot tables are derived from picks of the first breaks of over 200 VSP records. We create images of the fracture planes through two of the hydraulically fractured wells in the field. The scattered energy shows correlation with the locations of the microseismic events. In addition, the azimuthal scattering is different from the azimuthal reflectivity of the reservoir, giving us more confidence that we have separated the scattered signal from simple formation reflectivity. Variation of the scattered energy along the image planes suggests variability in the quality of the fractures in three distinct zones.

Report Contributors:

D. R. Burns
R. Lu
M. N. Toksoz
K. Willis
M. E. Willis
Y. Zhang

Table of Contents

I. Executive Summary

Tight gas sand reservoirs generally contain thick gas-charged intervals that often have low porosity and very low permeability. Natural and induced fractures provide the only means of production. The objective of this work is to locate and characterize natural and induced fractures from analysis of scattered waves recorded on 4-D (time lapse) VSP data in order to optimize well placement and well spacing in these gas reservoirs. Using model data simulating the scattering of seismic energy from hydraulic fractures, we show that it is possible to characterize the quality of fracturing based upon the amount of scattering. Two modeling approaches were used: 3D elastic finite difference modeling and a point-scatterer kinematic approach. The finite difference models were run for single and multiple hydraulic fractures. The results indicate that the scattered wave amplitude is a function of the fracture compliance, which can be related to the flow capacity or 'quality' of the fracture. The moveout of synthetic microseismic events were used to extract stacking operators that allowed individual fractures to be analyzed even when scattering from multiple fractures was present. The kinematic point scatterer models showed that the best fracture images from scattered wave time-lapse data were obtained when the VSP shot points covered a wide azimuthal range. Therefore, acquiring data with an azimuthal arc of shot locations was preferred to linear walk-away VSP geometries.

The 4d VSP methods developed and tested on synthetic data sets were then applied to a field dataset from the Jonah Field in Wyoming to characterize the quality of the hydraulic fracture stimulation program in several wells. The time lapse (4D) VSP data from this field are imaged using a migration algorithm that utilizes shot travel time tables derived from the first breaks of the 3D VSPs and receiver travel time tables based on the microseismic arrival times and a regional velocity model. Four azimuthally varying shot tables are derived from picks of the first breaks of over 200 VSP records. We created images of the fracture planes through two of the hydraulically fractured wells in the field. The scattered energy shows correlation with the locations of the induced microseismic events recorded during the fracturing treatment. Variations on these fracture plane images may reveal the changes in fracture quality. Three fracturing zones were observed in the final images: 1) the deepest zone showed good scattering within 50 m of the borehole, 2) the intermediate depth zone shows good and moderate scattering out to about 300m, and 3) the shallowest zone showed limited scattering. Limited production information indicates that the intermediate depth zone may be the most productive, suggesting that the deep zone has good fracturing, but only near the well bore; the intermediate zone has good quality fractures out to about 300m; and the shallower zone has poor quality fractures. More analysis of the images, microseismicity, and production data are needed to understand these relationships more fully.

II. Introduction

In order to determine the extent of hydraulic fracturing away from the injection well, micro-earthquakes induced during the fracture stimulation are recorded in a nearby observation well equipped with multiple levels of three component, clamped seismometers. The P and S-wave arrival times of these events are picked in near-real time, and the location of the fracturing is determined using standard earthquake location techniques. The microseismic events can be co-rendered with a 3D seismic volume so that the lateral and vertical extent of fracturing can be visualized with interpretations of the reservoir unit. The hydraulic fracture program can be modified, based on the microseismic event locations, to try to ensure that the fractures are only occurring in the reservoir unit and not propagating into the cap rock or a previously fractured compartment, for example. The effectiveness or quality of the fracturing is then measured by actual flow back tests into the well bore. While these tests can determine the overall success, it is currently not possible to isolate which specific portions of fractured rock volume are productive. The purpose of our research is to investigate whether these induced fracture systems scatter seismic energy that can be observed in a 3D, time lapse VSP survey and analyzed to provide diagnostic information about the effectiveness of the fractures. We first summarize a model study which is motivated by a field data set from a tight gas field which was collected in the same manner as our model, i.e. a time lapse VSP and microseismic recordings of a hydraulic fracturing treatment. The microseismic events provide us with the locations of the fractures within the VSP imaged volume, and the relative amplitudes of the P and S wave scattering in the VSP data will hopefully provide a measure of the fracture properties.

Conventional 3D VSPs are used to obtain high-resolution reflection images of the area immediately surrounding the borehole. The VSP seismic energy only travels essentially one way, from the surface through the subsurface and into the borehole. It does not travel back to the surface again. Because the energy is traveling one way, the bandwidth of the VSP signal is usually much wider than surface seismic data because it has not suffered as much attenuation.

The purpose of our VSP processing is not to examine the subsurface reflectivity. Rather, we are only interested in the changes associated with the introduction of fractures into the subsurface reservoir. In particular, we are looking for scattered seismic energy off of the hydraulic fracture planes themselves. Thus, the 3D VSP collected before the hydraulic fracture treatment contains the reference, or background, reflectivity. After the hydraulic fracture treatment, multiple sets of fractures have been introduced into the formation at specific, controlled depth levels. The microseismic events associated with the hydraulic fracturing reveal the precise location of the fractures. Because the new fractures are expected to be roughly planar, and generally follow the maximum stress orientation, the gross volume properties of the formation are not changed to a significant level. This means that the formation velocity stays relatively the same and it is possible to subtract the reference, i.e. before, VSP from the after treatment VSP survey. This difference is called the time-lapse survey.

The goal of the hydraulic fracture treatment is to create new pathways for fluid flow in the formation. Proppant is pumped into the formation simultaneously with the fracturing fluid. In the locations where the proppant is deposited, the hydraulic fracture will remain open after the high fluid pressure is released. Thus it is expected that in locations along the fracture plane where proppant is deposited, the compliance of the hydraulic fracture plane will be larger than the background formation compliance. In other areas without proppant, the fracture is likely to be closed and the difference between the formation and fracture compliances will be small. The ability of the induced fractures to scatter seismic energy is directly related to the relative difference of the compliance of the fractures. This means that is it very likely that those locations where the proppant was deposited and the fracture planes are open are the places which will scatter the seismic energy and therefore will be recorded in the after treatment VSP.

The arrival times of the microseismic events at the borehole receivers are extremely useful because they mimic the moveout of the scattered seismic energy in the after treatment VSP survey. Figure 1 (from Willis et al., 2007) shows an idealized acquisition experiment for a five layer model containing a single fracture. The vertical blue line shows the location of a monitor well containing multiple levels of clamped geophones. The red stars on the surface denote the locations of surface VSP sources. The black subsurface rectangle shows the location of a fracture plane. Figure 1a shows the ray path of the seismic energy (in the red line) from a single surface VSP source to the fracture plane. Scattered energy off the fracture plane to the monitor well geophones is shown by the blue lines. Similarly, Figure 1b shows the ray path for seismic energy from a single microseismic event to the monitory well in blue lines. We see that the scattered VSP energy from the location of the microseismic event follows the same travel path from the fractures to the monitor borehole that the microseismic energy follows. Thus, the picked arrival times of both the P and S waves of the microseismic events provide stacking operators we can use on the time lapse VSP data to extract and characterize the scattered seismic energy from the fracture planes.

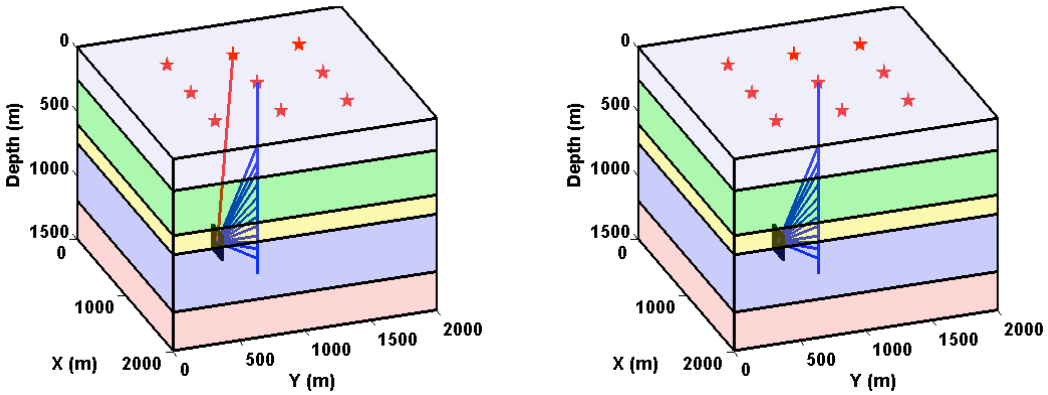

Figure 1. a) Conceptual ray paths for seismic energy scattered off the fracture plane from a surface VSP source. Surface source is the red star, the red line denotes the seismic energy traveling from the surface source to the fracture plane (black), and the blue lines show the ray paths of the scattered energy off the fracture plane back to the monitor borehole (vertical blue line). b) Conceptual ray paths (in blue lines)

for the microseismic events coming from the fault plane (black rectangle) to the monitor well (vertical blue line). Modified from Willis et al. 2007.

III. Elastic Finite Difference Modeling

We first created finite difference model data to simulate the effects of fracture compliance on the scattered seismic wave field. We reported our single fracture work in Willis et al. (2007). Here we extend that model to include two fractures. To create synthetic VSP records, we used a 3D elastic finite difference algorithm based on the rotated staggered grid method (Saenger and Bohlen, 2004; Zhang et al., 2006). The geometry of the two-fracture model is shown in Figure 2. The single fracture model is the same except that the upper fracture is omitted. Both models consist of five horizontal layers, with the velocities shown in Table 1. All the layers are homogeneous and isotropic elastic media. For the two-fracture model, layers 2 and 4 each contain a single hydraulic fracture. For the single layer model, only layer 2 contains a fracture. Each fracture is represented by specific grid cells containing equivalent anisotropic medium parameters using the method of Coates and Schoenberg (1995).

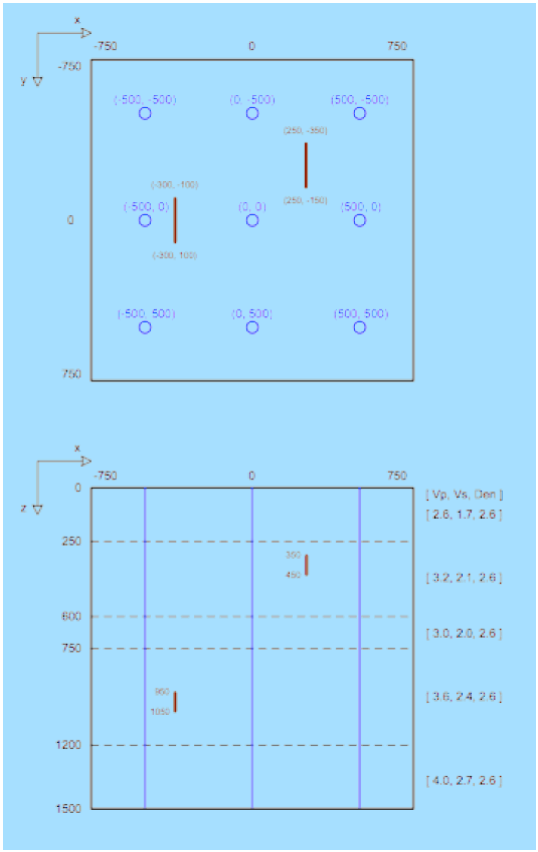

Figure 2. Model geometry for the case with two fractures (red lines) located at different spatial positions. The top panel shows the map view with the blue circles representing the surface source locations and VSP well locations. The bottom panel is the side view (depth) showing the different layers, velocities and densities. For the synthetic results shown in later figures the receivers are located below the center blue circle in the top panel.

Layer	Vp (km/s)	Vs (km/s)	Density (g/cc)
1	2.6	1.73	2.6
2	3.2	2.13	2.6
3	3.0	2.0	2.6
4	3.6	2.4	2.6
5	4.0	2.67	2.6

Table 1. Layer parameters for the five layer model shown in Figure 3. Layer 1 is the shallowest layer.

In a fashion similar to Figure 1, we show the ray paths for the two-fracture model in Figure 3. The left panel (a) shows the ray paths for the VSP source energy from the surface shot to the fracture and then to the geophones in the monitor well. The right panel (b) shows the ray paths for the microseismic energy. The ray paths displayed are conceptual in nature and do not depict the actual ray bending through the model because we are only trying to demonstrate the concept that the scattered energy travels the same path as the microseismic energy. (The actual ray paths would bend at the layer boundaries for both wave fields; this effect is not important for this discussion.)

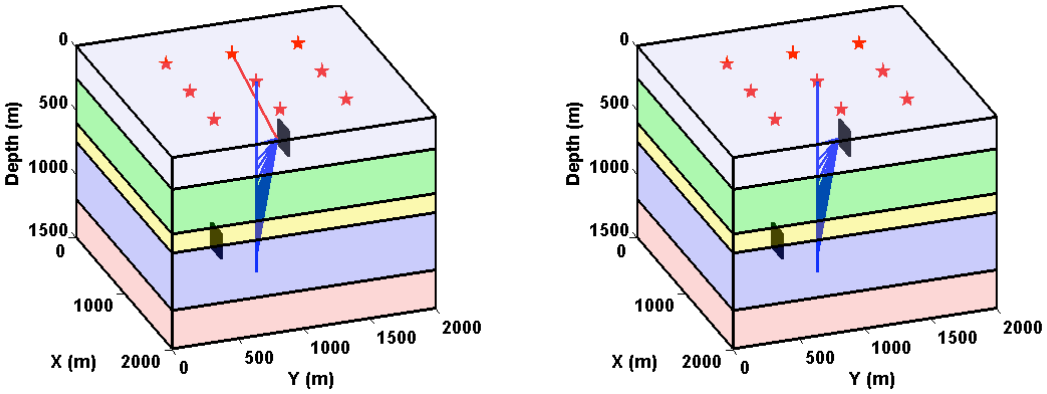

Figure 3. a) Conceptual ray paths for seismic energy scattered off the upper, shallow fracture plane from a surface VSP source. Surface source is the red star, the red line denotes the seismic energy traveling from the surface source to the upper fracture plane (black), and the blue lines show the ray paths of the scattered energy off the upper fracture plane back to the monitor borehole (vertical blue line). b) Conceptual ray paths (in blue lines) for the microseismic events coming from the upper fault plane (black rectangle) to the monitor well (vertical blue line).

We model a microseismic event in the middle of the lower fracture plane using the same finite difference modeling algorithm and different source mechanisms to represent the event. For simplicity of presentation, in Figure 4 we show the Vz component for an

explosive source. Of course this is not realistic for the dynamics of a microseismic event, but the kinematics of the arrival times are identical to those for a more complicated source mechanism.

For the study we presented in Willis et al. (2007) we generated the VSPs for the single fracture model in Figure 1 and one containing no fractures. A time lapse (4D) VSP record was created by subtracting corresponding VSP shot records from both the fracture and no fracture modeled data sets. Figure 5a shows one of the Vz time-lapse VSP records from that study. We repeated this same procedure for the two-fracture model and created the corresponding time lapse VSP record in Figure 5b. Clearly present on both records is the arrival of P wave, with the fastest moveout, and S wave energy, with the slower moveout. The long time duration of the scattered waves is caused by the finite size of the fracture plane, which shows scattering from all of its edges in addition to its face.

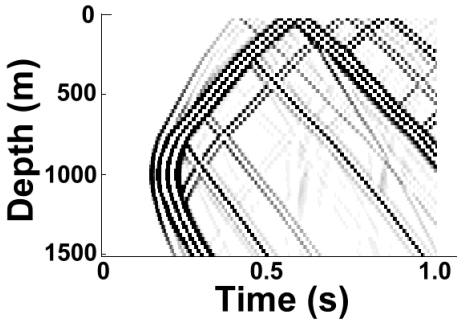

Figure 4. Modeled microseismic event at center of lower fracture.

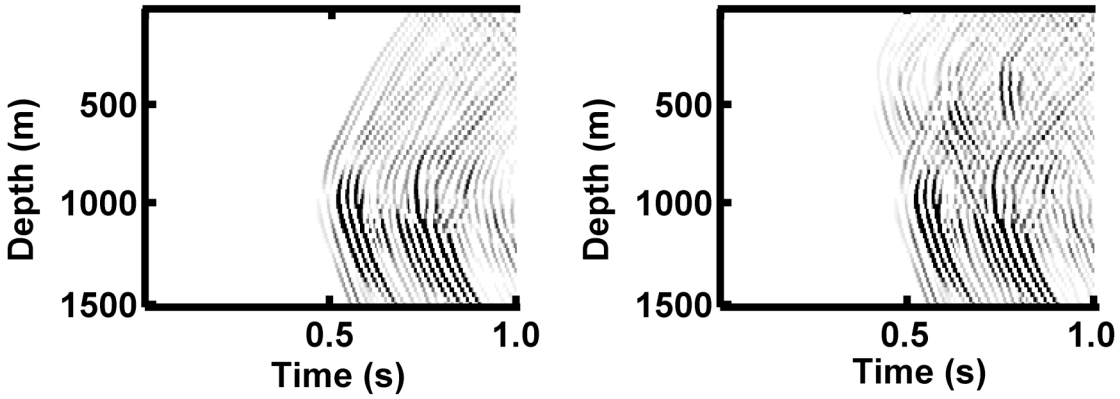

Figure 5. a) Modeled time-lapse VSP record for single fracture model. b) Modeled time-lapse VSP record for two-fracture model. Both records show Vz motion.

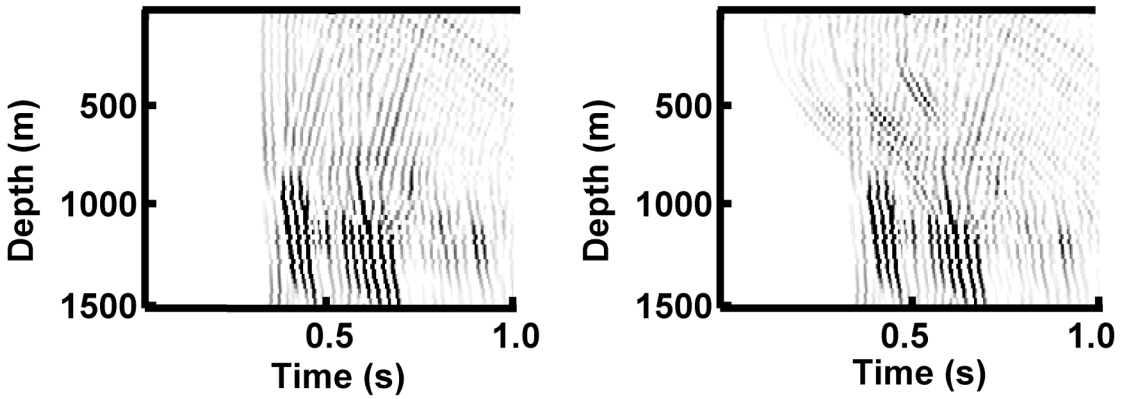

Figure 6. a) Modeled time lapse VSP record for single fracture model (in Figure 5a) shifted by the moveout of a microseismic event on the lower fracture plane. b) Modeled time lapse VSP record for two-fracture model (in Figure 5b) shifted by the moveout of a microseismic event on the lower fracture plane. Both records show Vz motion. The moveout of the microseismic event was hand picked from the modeled waveforms. Note the P wave arrival of the scattered energy from the lower fracture plane is aligned vertically, allowing it to be separated from the upper fracture plane energy.

The arrival times of the modeled microseismic event (e.g. in Figure 4) at each geophone in the monitor well was hand picked and recorded. These times were then used to reduce (i.e. time shift to align) the traces of the corresponding time-lapse VSP records. An example of time shifting the traces in Figure 5 is shown in Figure 6 using the microseismic P wave arrival times. In Figure 6a, the single fracture model shows that the scattered P waves are aligned in time, and the S waves show a significant residual moveout. Figure 6b shows the same operation applied for the two-fracture case. Now we see that the scattered energy from the upper fracture is not aligned, and the lower fracture P wave energy is clearly aligned. These time-shifted traces can then be stacked and used to measure the amount of scattered energy for that specific wave type from the location of that microseismic event.

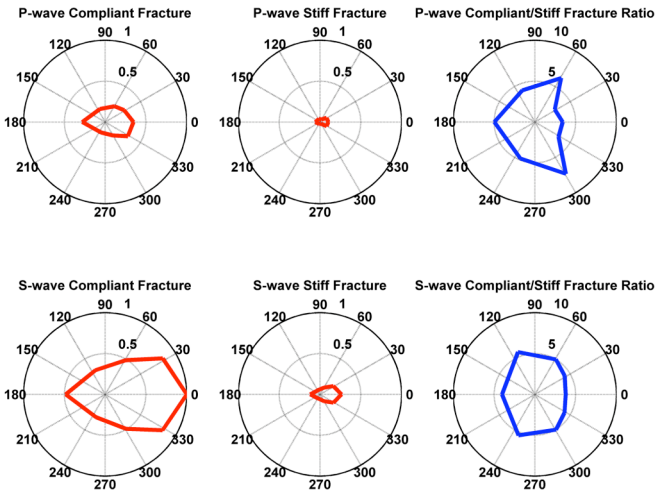

Figure 7. Scattered seismic energy from a modeled time lapse VSP data set. The left column of polar plots shows the amount of coherent scattered energy for a compliant (open) fracture while the middle column shows a stiffer (more closed) fracture. The right column shows the ratio of the compliant to stiff energy. The top row of polar plots shows the scattered P wave energy, while the bottom row shows the scattered S wave energy. In each polar plot, the amount of scattered energy is shown as a function of the angle that the source makes to the projection of the normal to the fracture surface onto the surface of the earth. Thus zero degrees indicates where the surface source is normal to the strike of the fracture plane. Modified from Willis et al., 2007.

In a 3D VSP survey, the target fracture zone is illuminated from many incident directions, since the surface seismic sources cover a large area over the subsurface fracture plane. Thus the amount of scattered energy can be determined for many azimuths around the fracture plane by sequentially stacking the time-shifted traces for each time lapse VSP surface shot location. Willis et al. (2007) presented the scattered P and S wave energy for two different single fracture models, reproduced in Figure 7. The left column of polar plots shows the amount of scattered energy for a very compliant (or open) fracture. The middle column of polar plots shows the scattered energy for a stiffer (or more closed) fracture. The top row shows the amount of P wave scattered energy while the bottom row shows the amount of S wave scattered energy. From Figure 7 it is clear that the models suggest that more S wave energy is scattered than P wave energy. Also shown is that compliant (open) fractures scatter more energy than stiff (closed) fractures, and that the most scattered energy is generated from shots that are normal to the fracture strike.

While it is impossible to characterize the rock volume associated with each microseismic event, it may be feasible to compare the relative scattering for small rock volumes, perhaps as small as 10m on a side, across the reservoir. While the actual properties of the fractured zone itself may prove difficult to estimate, we should be able to map the areas with relatively higher fracture quality, i.e. open and compliant properties, based upon the amount of seismic scattering.

IV. Point Scatterer Acquisition Modeling

Traditional imaging methodologies have well developed criteria for specifying the acquisition effort required to image the subsurface. For scattered energy on time-lapse seismic data, no such criteria exist. The goal of this section is to explore different surface VSP source configurations and the subsequent imaging power required to resolve point scatters in time-lapse data. This will provide guidance on what VSP shot locations should be used for imaging fracture quality.

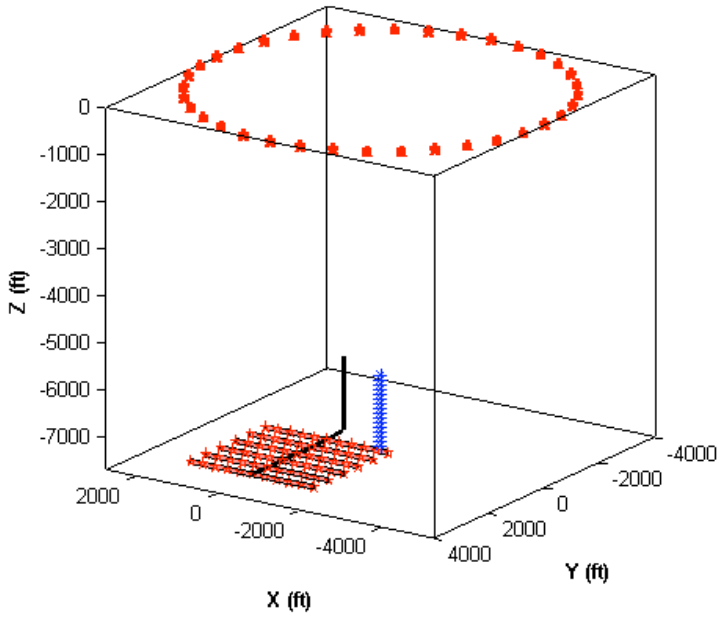

Figure 8. Model containing 6 hydraulic fractures, shown by the horizontal black lines. On each fracture there are 11 point scatterers, which simulate the scattering from the fracture plane. The monitor well contains 16 receivers (in blue) that are spaced apart by 100 ft.

To address this question, we created a simple point scatter model consisting of several closely spaced hydraulic fractures. Figure 8 shows the model, which contains 6 hydraulic fractures that are each 3000 ft long. Each hydraulic fracture is composed of 11 point scatterers. There are 16 receivers in the monitor well, spaced 100 ft apart. An example of a circle of surface VSP source points is shown by the red stars. Figure 9 shows an example modeled time lapse record for P-waves only for a surface VSP source located at the left edge of the model (x=2700 ft, y = 0 ft). All of the scattered energy, modeled by single scattering, merges into a jumbled set of events.

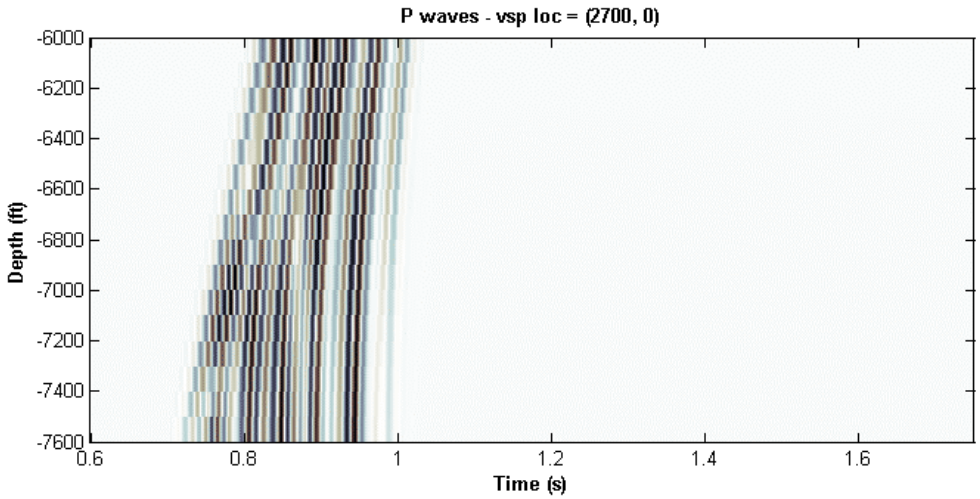

Figure 9. Example time-lapse VSP record containing P waves only for the model in Figure 6.

We could use 3D prestack depth migration on this data to create a fully migrated 3D volume of scattered energy. To do this on field data, however, would require a very accurate velocity model. Since the scattered waves will be travelling mostly in the horizontal direction, they will be most sensitive to the horizontal P and S wave velocities. Unfortunately, the velocities measured by traditional VSP processing methodologies are mostly influenced by the vertical velocities. Since we expect that the amplitudes of the scattered waves will be small, it is very important to use the best estimate of the horizontal velocities available. Without accurate velocities it will be impossible to extract each fracture signal from the jumble of interfering scattered waves. Because the microseismic events propagate along this horizontal travel path, they contain the best velocity information possible about the scattered field.

To process these model data, we create stacked traces corresponding to the scattering points all along each of the hydraulic fractures. We migrate each time lapse VSP trace to a series of locations along each hydraulic fracture. As stated above, we could just use a velocity model and perform conventional migration. However, we choose to use the microseismic event moveout to stack the trace. We still need to know the travel time from the surface VSP source location to each point on the hydraulic fracture. For this, we use ray traced travel times. We then add to this the moveout times from the measured microseismic events.

Figure 11 shows an example set of migrated and stacked traces for the first stage of fracturing in Figure 10. The vertical axis is in time. In a traditional depth migration we would have only created a single sample for each point in x, y, and z on the fracture plane. Here we have computed the stacked trace, which is equivalent to creating the redatumed trace at the fracture. Thus, the sample at zero time corresponds to the migrated sample at the fracture. Negative time contains the wave field that has already focused at an image point above the fracture, and positive time corresponds to the wave field that will collapse at a deeper location. Thus, if we observe a wavelet, which is centered at the zero time lag location, we have correctly imaged this contribution. From this figure we see that the variation in the burnt orange color at zero lag shows that the imaging has not perfectly constructed the uniform scattering field used in the model. We will form a stacked image of each fracture plane as shown in Figure 12.

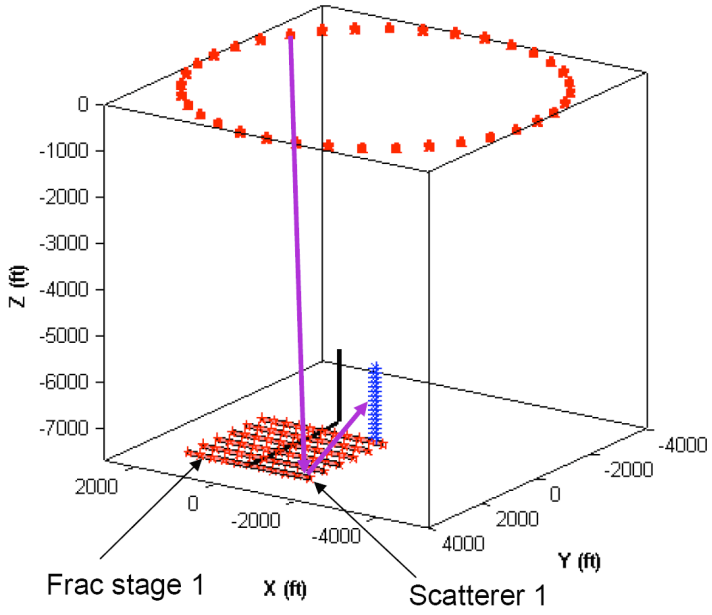

Figure 10. Diagram showing ray path (in purple) from a surface VSP source (red star) to the first scattering point on the first hydraulic fracture (stage) and then to a receiver (blue cross) in the monitor well.

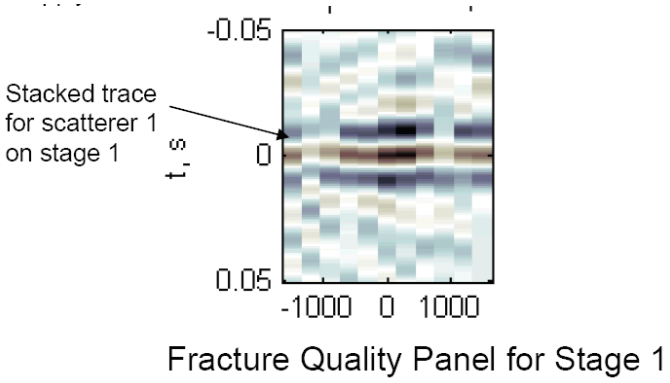

Figure 11. Migrated, stacked traces created for the first stage of fracturing of the model shown in Figure 10. The left most trace (at -1500 ft) corresponds to the first scatterer in Figure 10. The vertical axis is time in seconds, while the horizontal axis is distance along the fracture in ft.

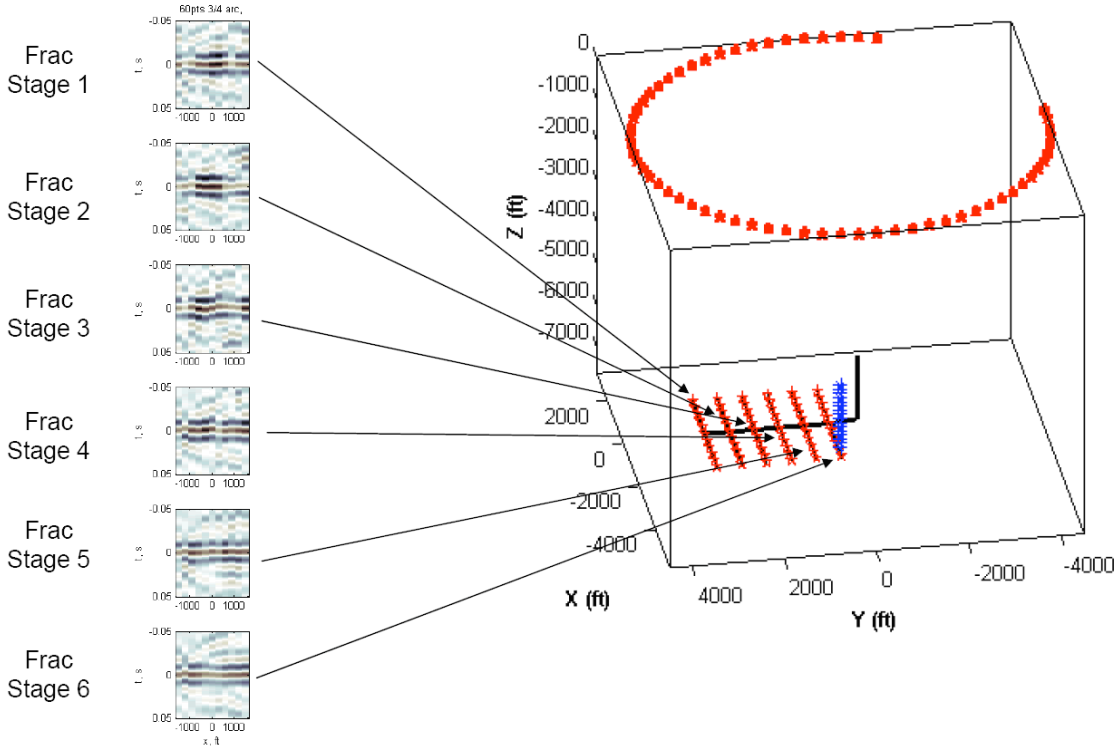

Figure 12. Diagram showing the relationship between images of the modeled hydraulic fracture planes (left) with their actual location in the model (right). In this example the VSP sources form a ¾ circle on the surface.

We next analyze the imaging capabilities of several groupings of surface VSP sources. Here we are looking to characterize the imaging resolution of the method on a controlled set of experiments. We need to be able to quantify the resolution of the method so that we have a sense of precision of the method to detect changes in amplitude. Figure 13 shows six different groupings of surface sources. Obviously there are a very large number of combinations of surface sources that could be used for imaging.

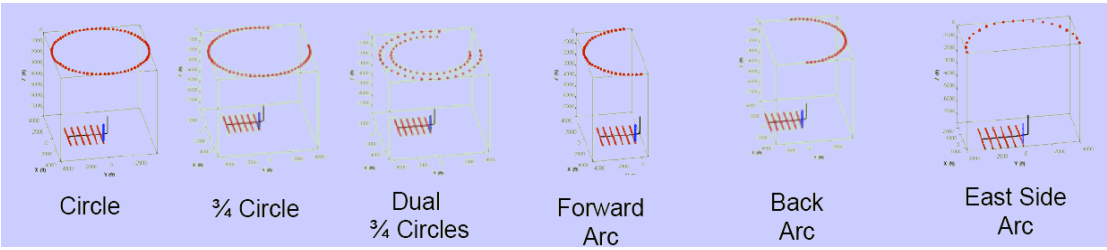

Figure 13. Six different sets of surface VSP sources used for analyzing their imaging effectiveness.

The first pattern analyzed is the circle. It seems to be an obvious choice because it illuminates the target equally from all directions. The next pattern is the ¾ circle design. With it we investigate the effect of missing a portion of the complete coverage. The dual ¾ circle design is perhaps very similar in many ways to the actual acquisition pattern. The field data set described below has an acquisition pattern that is missing source coverage in the southeast portion of the survey. While the actual acquisition pattern is not 2 circles, the dual circle design has many of the same traits. The next three patterns

split the circular design into half circles (or arcs) that illuminate the fracture planes from the forward, back, and side scattering viewpoints. Figure 14 shows three more patterns. The bow pattern consists of a rotated half circle. The long arrow pattern is a single line that traverses the fractures at a 45-degree angle. The bow and long arrow pattern combines these last two patterns.

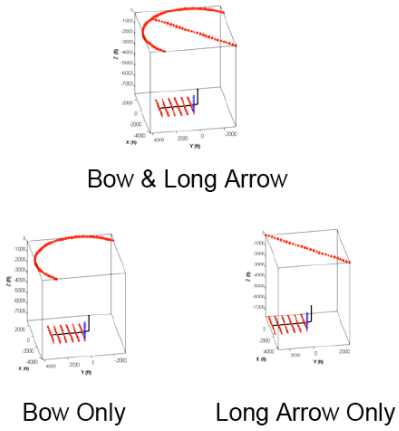

Figure 14. Three additional sets of surface VSP sources used for analyzing their imaging effectiveness.

We have modeled the acquisition using both P and S waves but we show only the P wave result here. The model uses a constant velocity for P waves (11,900 ft/s or 3627 m/s). However, because it is not known exactly how hydraulic fractures scatter seismic energy, and because 3D finite difference elastic modeling is expensive and time consuming to perform, we analyzed three different radiation patterns for the point scattering representing uniform, dipole, and clover shape. Here we show the imaging results using the uniform or omni-directional scattering model, which creates an equal amount of energy in all directions. The result for uniform scattering is similar to, although slightly better than, those for the dipole and clover radiation patterns.

The imaging simulation uses P wave energy only, and point scatterers distributed on the fracture planes as shown in Figure 8. Each fracture is 3000 ft in length and is approximated by 11 point scatterers with omni-directional scattering with equal amplitudes. Thus the model contains a total of 66 point scatterers. The radius of the (outer most, if applicable) source arc is 4250 ft. The migrated stacked traces are shown in Figure 15. Each column represents the imaging results using the VSP sources shown in the pattern in the diagram at the column heading. Each row represents the image obtained for that fracture stage listed at the row heading. Thus the image in the first row and column represents the migrated stacked image using the circular pattern of VSP sources for the first fracture stage. This is the fracture that is the farthest from the monitor well as shown in Figure 8. The image shown in the first column and last row represents the result for the fracture closest to the monitor well using the circular source pattern.

The imaging results for the circular source patterns (columns 1 through 3) and the back scattered arc (column 8) appear to give the best (i.e. most uniform) images. The single line or long arrow (column 6) and the bow combinations (columns 4 and 5) seem to perform the worst. From both the P and S wave modeling, with three different radiation patterns of scattering, it appears that the best images are provided by acquisition geometries which provide illumination from surface sources which almost surround the fracture(s). Thus when selecting which surface sources to use in creating images of the fracture plane, it is best to select circles instead of single lines or semi-circles.

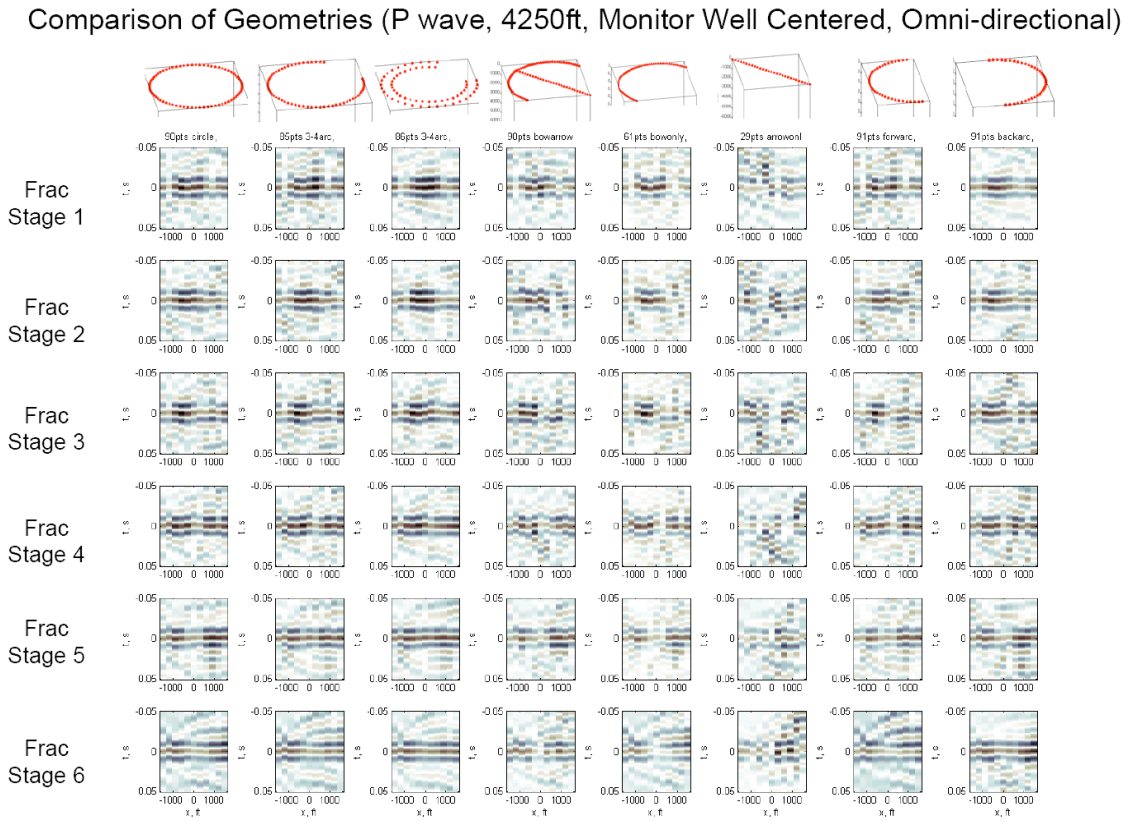

Figure 15. Migrated stacked panels for each of 8 sets of VSP source patterns (shown in column headings across the top) for all 6 fracture stages (shown as the row headings). P wave only energy was used with an omni-directional scattering radiation pattern.

V. Field experiment

The Jonah Field is a tight gas field located in Sublette County, Wyoming. The field is defined by a wedge shaped structural block created from the intersection of two subvertical shear fault zones. The reservoir is comprised of the sandstones of the Lance Formation, which are meandering stream channels intercalated with overbank siltstones and mudstones (DuBois et al., 2004). The gross thickness of the reservoir can be in excess of 900m. Despite high reservoir pressures, production is difficult due to low

permeability requiring extensive, multi-stage hydraulic fracturing to produce economic quantities of hydrocarbons.

A map of the survey area is shown in the left panel of Figure 16. The black dots show the layout of the surface seismic sources used in the time lapse VSP survey. The red dot shows the location of the monitor well that was instrumented with clamped geophones. Hydraulic fracturing was performed in five wells during this treatment program. Since the wells in this area are tightly spaced in order to reduce the surface impact, wells are typically spudded from a limited number of surface pads and are then horizontally deviated to hit their subsurface targets. The two blue dots show the bottom-hole locations of the two wells used in this study. The green dots show the bottom-hole locations for three additional wells that were also fractured during the treatment program.

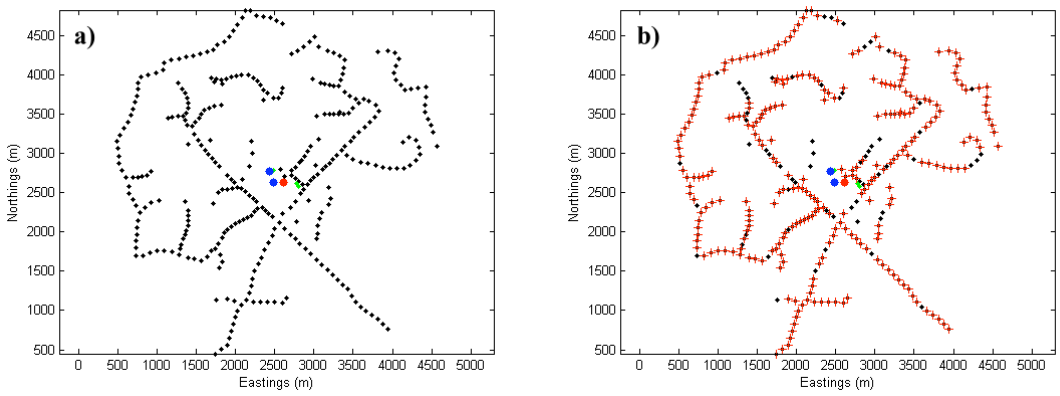

Figure 16. Maps of test area in Jonah Field showing a) all shot locations and b) highlighting the good shots with red crosses. The red dot shows the location of the monitor well which recorded the time lapse VSPs and the microseismic events. The two blue dots show the bottom hole locations for the two hydraulically fractured wells studied in this paper. Well A is North and slightly West of Well B. The three smaller green dots show the bottom hole locations for other wells that were hydraulically fractured contemporaneously. The black dots show the locations of the 338 surface seismic sources used for the time lapse VSP survey.

Before the treatment program began, a 3D reference VSP survey was recorded over the field using 338 surface shot locations. During the different time periods of acquisition, an OYO DS250 tool string with either eleven or twelve levels and a fiber optic wireline was used to record the VSP data. The tool was progressively moved up the monitor borehole to record a total of 140 VSP levels. Then the hydraulic fracturing was performed. The lowest portion of each of the 5 wells was fractured successively. For this stage of fracturing, the clamped geophones in the monitor well were placed near the depth level of the hydraulic fracturing to straddle the fracture zone. Then the geophones were raised to accommodate the depth level of the next shallower fracture stage. As many as twelve stages of fracturing in each well were recorded. About a month after the original 3D reference VSP survey was collected and after the hydraulic fracturing was completed, a second 3D VSP survey was collected over the field using the same surface shot locations and the same nominal subsurface depth levels.

The microseismic events were picked and located by Pinnacle Technologies. Due to the proximity of the monitor well and the data quality, the most reliable microseismic events appear to be obtained from wells A and B, which are shown as the blue dots in Figure 8.

VI. VSP time lapse processing

A purpose-built processing system was created to analyze and process the two 3D VSP surveys in order to create the time lapse VSP data volume. The first step was sorting and matching the geometries of the two surveys. The bandwidth of the field data seemed to exceed 130 HZ, but closer inspection showed that the reliable and repeatable portion of the band was below about 50Hz. Thus the data was filtered to retain full fidelity between 15 and 70 Hz. Several depth levels showed evidence of poor clamping and they were removed from the analysis. All 676 VSP records were examined and noisy traces were manually edited out.

True amplitude recovery was accomplished by applying a correction for spherical divergence of the form t^n, where t is the time down the trace and n is an exponent that is normally chosen to be between 1 and 2. Visual inspection of the data confirmed that an exponent of n=1 was optimal to balance the amplitudes on the traces.

The next step was the application of amplitude and phase matching between the surveys. The overall static gain between the two surveys was different by a factor of over 1000. In addition to the static gain, any wavelet change between the reference VSP source and the after fracturing VSP source will introduce time and amplitude distortions.

In our first attempt to correct for this effect, we created a phase and amplitude correction filter for each shot point. For each shot point, a first arrival mute was manually designed to isolate the theoretically identical portion of the traces. The mute began slightly before the direct arrival and persisted for a small time window afterward, based on the assumption that the direct arrival on each trace is the best estimate we have of the combined source waveform and receiver effect. The VSP waveforms for the direct arrival should be nearly identical for both the before and after surveys. Therefore, we created the spectral ratios of the direct arrivals between the before (reference survey) and after (fracture treatment) traces. This spectral ratio contains differences in the source wavelet as well as receiver differences relating to changes in geophone clamping between surveys.

Assuming that the source wavelet does not change between the surveys, an overall source correction operator could be estimated in a surface consistent manner from the spectral ratios of all traces at all the shot points. Likewise, 140 individual receiver correction operators could be derived. However, since there might be small changes in the source waveforms due to changes in the vibrator pad coupling at each shot point, a simple correction for each trace was derived instead. Thus a correction operator was derived from the spectral ratios of each pair of traces, which forces each direct arrival in the after-fracturing survey to be identical to the corresponding reference survey direct arrival. The

correction operator was derived from the direct arrivals, but it was applied to the entire trace of the after-fracturing survey. A subsequent examination of the measured microseismic moveouts, however, showed that all of the microseismic arrival times are less than 100 ms. This means that on the 12-level tool, the depth levels closest to the hydraulic fracture will see the scattered energy arriving very close to the first breaks. Our spectral ratio method matching the surveys, therefore, may remove these arrivals since they will likely be within the window used to match the two surveys. To correct this problem and to compress the wavelet and ultimately match the two surveys, we applied a source deconvolution to both surveys instead.

To apply source deconvolution we first need to estimate the source wavelet. As in our initial spectral ratio approach, there might be only one wavelet for each survey. However, if the source varied at all due to ground coupling differences, then a different source wavelet should be used for each shot point. To estimate the source wavelet, we aligned the first breaks for each VSP and then stacked them. Thus each VSP shot point gives one stacked trace for each of the before and after-fracturing surveys. Figure 17a shows the stack of each of the 338 before-fracturing VSPs. The vertical axis is the shot point index number, and the horizontal axis is a 600 ms time window around the aligned time. We can see from this display that the source strength, i.e. amplitude, changes dramatically over the survey area. Also, the source wavelet changes as well. Figure 17b shows the same result for the after-fracturing VSP survey. For this display we have plotted the amplitudes with reverse polarity to match the before survey. Also note that the color bar reveals the factor of about 1000 difference in gain between the surveys. Figure 17c shows the extracted wavelet for the first breaks of the difference between the surveys. If the gains and phases were matched there should be only a very small signal on this panel. Note that we applied a polarity change to the after survey and a factor of 1000 to the before survey.

We used the extracted wavelets of the before and after-fracturing surveys to apply source decon. Source decon was applied using a simple spectral division approach where we damped the division with 1% white noise. Each VSP shot record had its corresponding source wavelet removed by spectral division. Using the same technique we used to estimate the source wavelet, we aligned and stacked the before and after-fracturing surveys again after source decon was applied. Figures 17d and 17e show the new estimated wavelets for the before and after surveys with source decon applied. Here we see that the shot-to-shot variation in amplitude has been virtually eliminated and the wavelet is very compact and zero phase. The corresponding stack of the difference with source decon (Figure 17f) reveals that this process has done a very good job of matching the two surveys, giving only a small amount of residual first break energy.

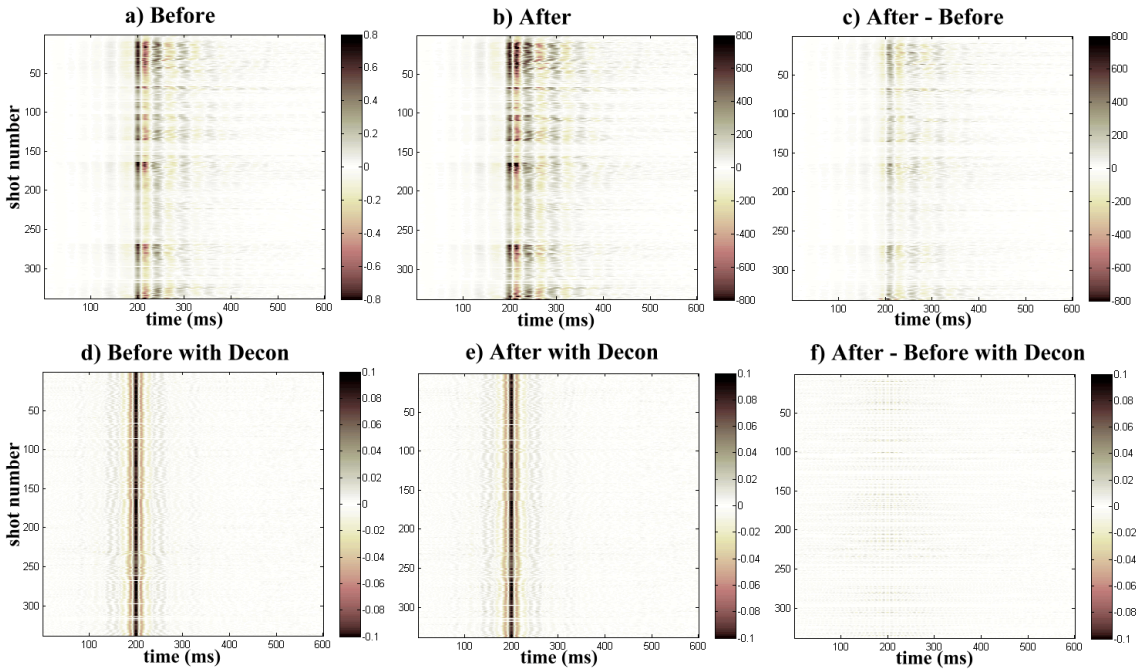

Figure 17. Source signature deconvolution results. The vertical axis in each panel is the shot number. The horizontal axis is time. The trace for each shot number is a time window 600 ms around the aligned and stacked first arrival in the VSP. Therefore, each trace is the sum of about 140 traces in the VSP. a) The stacked before survey. b) The stacked after fracture survey after applying a polarity change. c) The stack of the difference of the after and before surveys. d) The stack of the before survey after removing the corresponding source signature in a. e) the stack of the after-fracturing survey after removing the corresponding source signature in b. e) the stack of the difference of the after with decon and before with decon surveys.

An example of the results of source decon is shown in Figure 18. The top panel shows the VSP record after source decon was applied to the before-fracturing VSP. The middle panel shows the after-fracturing record, and the bottom panel shows the optimized difference. (The optimized difference process is described below.) Figure 19 shows the same record after a mute was applied to remove the first breaks.

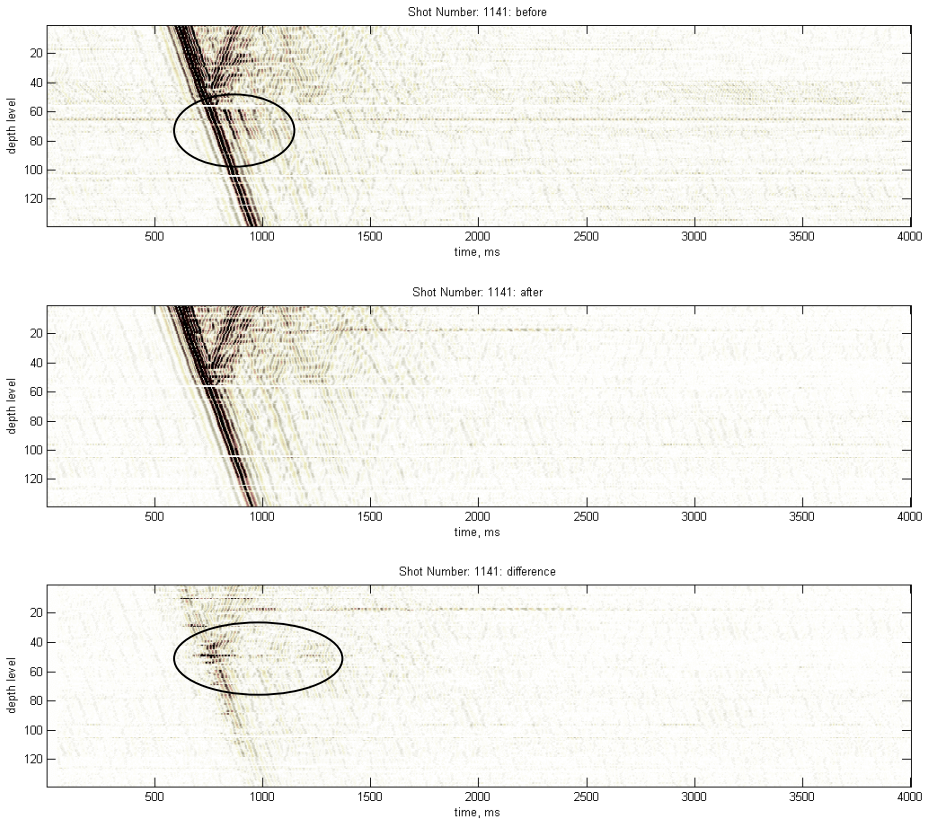

Figure 18. Example VSP records after source deconvolution. (Top) Before-fracturing, (middle) after-fracturing, (bottom) optimal difference. Notice the additional events following the direct arrival (circled) in the top panel.

The difference record in the bottom panel of Figures 18 is not entirely free of the direct arrival energy. Some of this is due to problems in the raw records themselves. Notice that between depth levels 60 and 80 on the before-fracturing record (top), there are two additional large amplitude events (circled in the figure) that are not present on the rest of the record and are absent altogether on the after record. This is an indication of some potential mix up in the original stacking or correlation process in the raw field records. Figure 20 and 21 show two more shot locations with similar problems. We have attempted to omit shot points with records like this one in the final analysis, which accounts for roughly 10% of the survey. However, we don't know the problem that caused these issues, and additional problems may exist in the records that we cannot visually detect. The red crosses in Figure 16b show the locations of the shot points that passed our visual inspection and are used in the analysis.

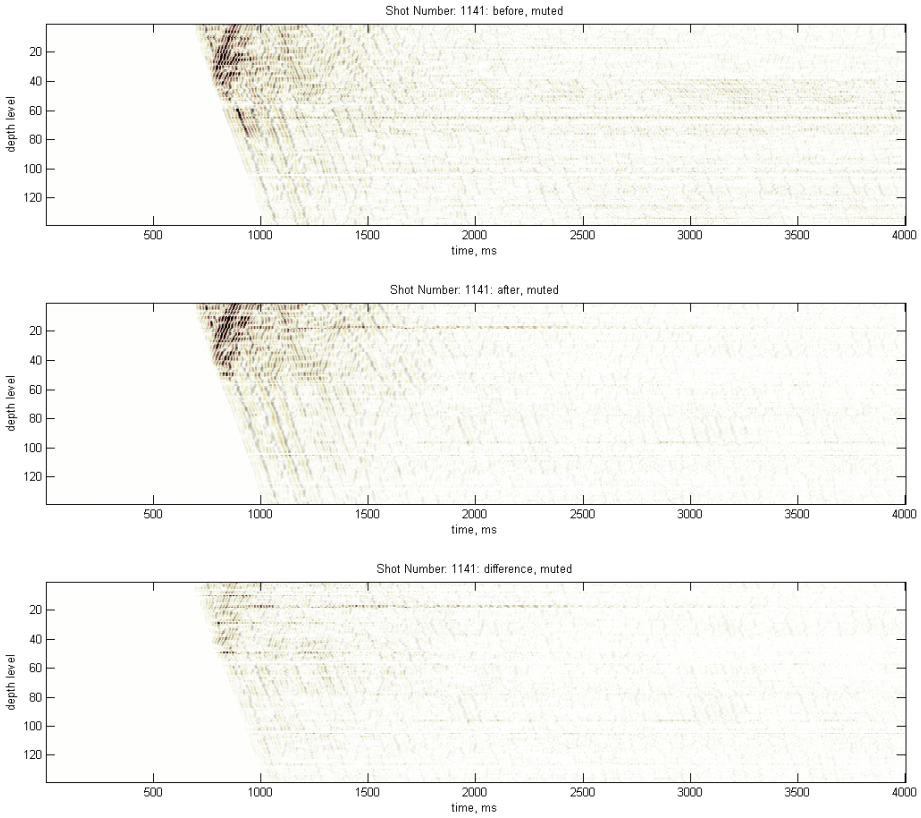

Figure 19. Example VSP records after source deconvolution and a mute to eliminate the first breaks. a) Before, b) after, c) optimal difference.

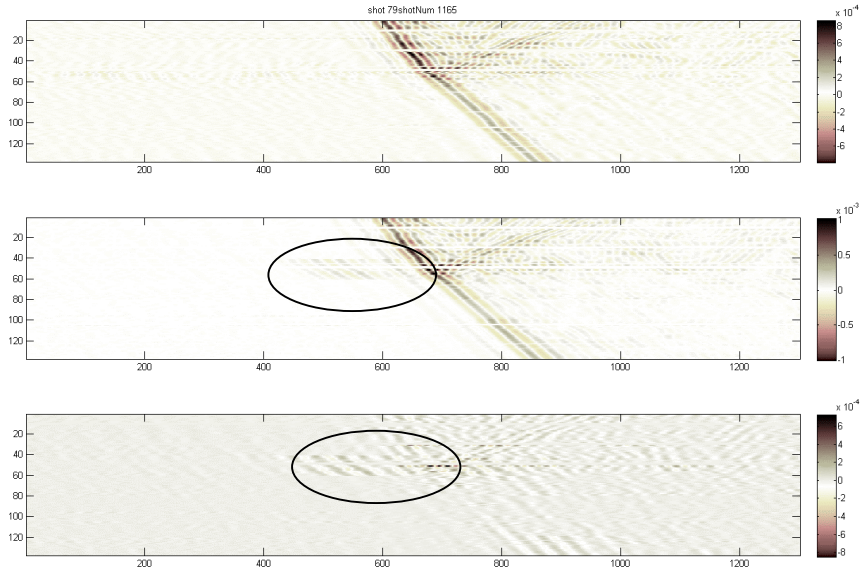

Figure 20. Example VSP records (shot index number 79) after source deconvolution showing data problems (circled) between depth levels 45 and 60. a) Before, b) after, c) optimal difference. Vertical axis is the depth level and the horizontal axis is time in ms.

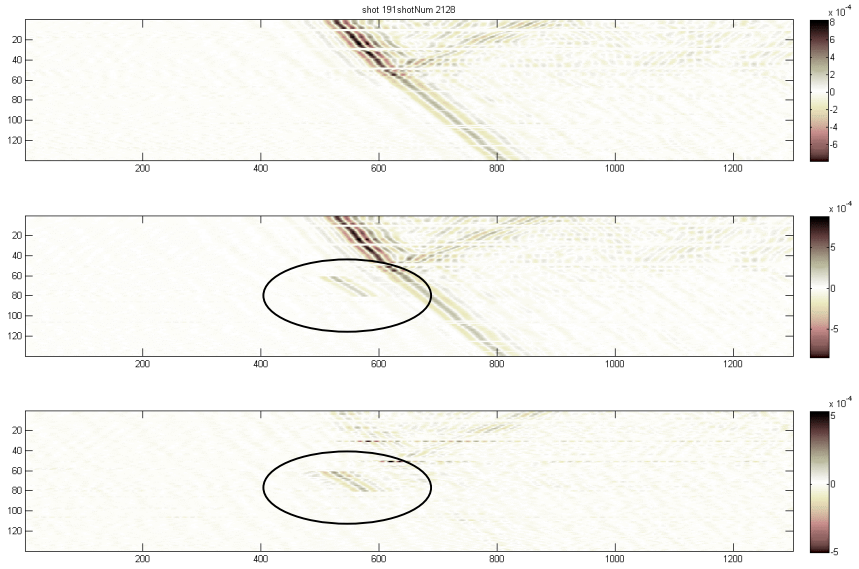

Figure 21. Example VSP records (shot index number 191) after source deconvolution showing data problems between depth levels 60 and 80 (circled). a) Before, b) after, c) optimal difference. Vertical axis is the depth level and the horizontal axis is time in ms.

The final preprocessing step is the creation of the time-lapse volume by subtracting the reference survey traces from the after-fracturing survey traces. This could be done as a simple subtraction. However, less noisy results were obtained from an optimal difference algorithm that used a sliding window down each trace. A scale factor was derived which minimized the root mean squared amplitude difference between the corresponding sample values in the sliding window. Thus each sample in the optimal time-lapse trace is created by deriving a scale factor to be applied to the reference trace samples in a sliding time window that minimizes the resulting difference. This process then attempts to match the two surveys in amplitude before taking the difference. Any small amplitude differences that are consistent over this time window will be removed. It is expected that this process will enhance scattered energy that is incoherent between surveys and reject small changes in amplitude caused, for example, by AVO-type effects.

We also tried to incorporate a time shift before subtraction. The idea behind this concept is that the fractures may introduce a small velocity reduction, causing a time delay of corresponding events. A straight subtraction of events that are slightly time delayed would cause a phantom event to be created. We are interested only the diffracted energy so this type of artifact would degrade our images. A sliding window was used and a cross correlation was applied to find the optimal time shift for that window. Unfortunately, this simple method without any constraints on the smoothness (or consistency) of the time shifts between time windows introduced high frequency "tears" in the difference signal. Thus the concept was discarded but may prove useful if a more robust implementation were created.

VII. Microseismic data

The microseismic events for each fracture stage were recorded and analyzed separately by Pinnacle Technologies to pick the arrival times. The perforation shots were also recorded for each of the wells to provide velocity calibration for the event location process. A different constant velocity (which was derived by analysis of the perforation shot data) was used for each fracturing stage.

The composite of all arrival time picks for Wells A and B are shown in the top and bottom panels, respectively, of Figure 22. Each line on the figure is for a single microseismic event picked on either 11 or 12 receiver depth levels. When the signal to noise ratio is not good enough to pick a time at one of the receiver depth levels, it is omitted. However, in this plot a straight line is used to "interpolate" those missing levels so that visually all the picks for each event can be tied together. There were twelve stages of fracturing in Well A and nine in Well B. For each stage the tool was moved for optimal coverage. Thus in the figure it is possible to see distinct groupings of arrival times associated with each time the tool is clamped into position.

It should be noted that just as in earthquake arrival time picking, the origin time of each microseismic event is unknown. Thus the times shown in Figure 22 represent the arrival time picks, which have been adjusted, based on the event location using the absolute arrival times, so that they are relative to the predicted origin time. In this way, events that are farther away from the monitor well are displayed at larger arrival times.

The velocities inverted from the perforation tests are shown in Figure 23a. Velocities are inverted for an interval in the monitor well of about 130 m. The velocity is decreasing with depth over this short interval from about 5500 m/s to 4900 m/s.

Once the events have been located using this velocity profile, it is possible to predict the arrival times at each of the receiver levels. Figure 23b shows the corresponding predicted arrival times for Well B using a constant velocity of 5182 m/s. These arrival times look visually more consistent because they are model based, and because the missing gaps which show as linear segments in Figure 22 have been interpolated through making smooth moveout curves. The point-by-point difference between the arrival times for Well B in Figures 22 and 23b would reveal the error and uncertainty of the time picks. The event locations for all of the fracture stages in all of the five wells are shown in Figure 24.

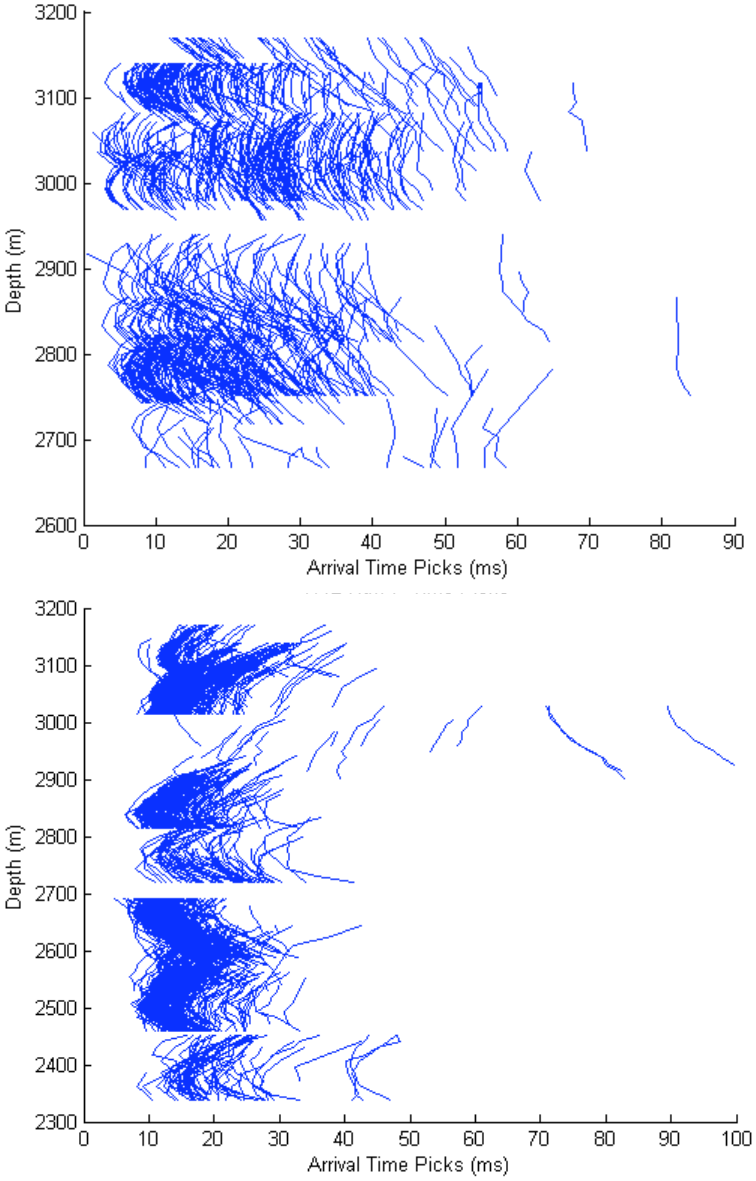

Figure 22. Arrival time picks for Well A (top panel) and Well B (bottom panel). Each line shows the time picks for a single microseismic event. The apparent depth segmentation of the picks is due to moving of the tool to be centered around the depth of the hydraulic fracturing of each stage. There were 12 depth stages for Well A and 9 for Well B.

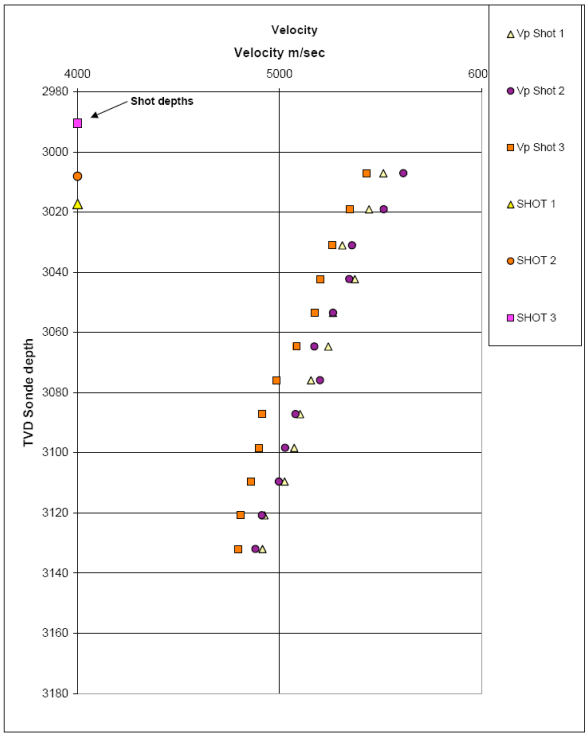

Figure 23a. Perforation shot tests for Well B. The depths of the three perforation shots are nominally shown at a dummy velocity of 4000 m/s. The inverted P wave velocity profiles are shown at each of the geophone depths by the points corresponding to the three shots.

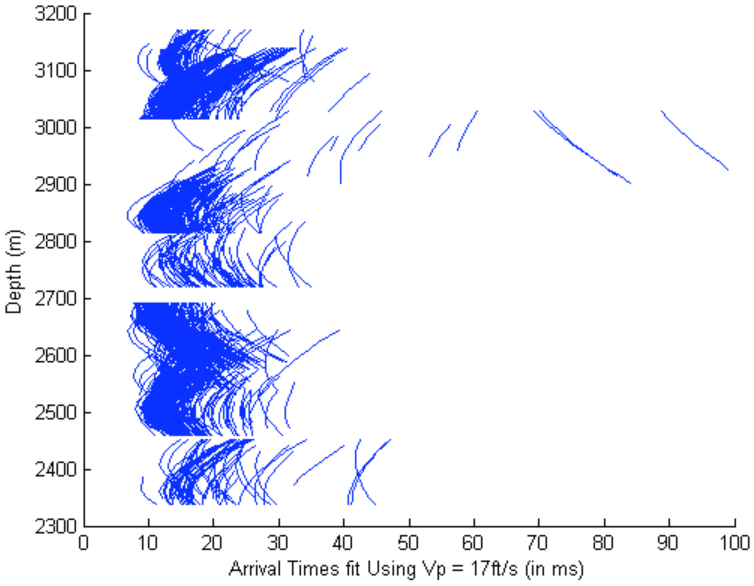

Figure 23b. Adjusted arrival time picks for Well B using a velocity of 5182 m/s. Each line shows the time picks for a single microseismic event. These times show the predicted arrival times after the actual arrival time picks are used to locate each event.

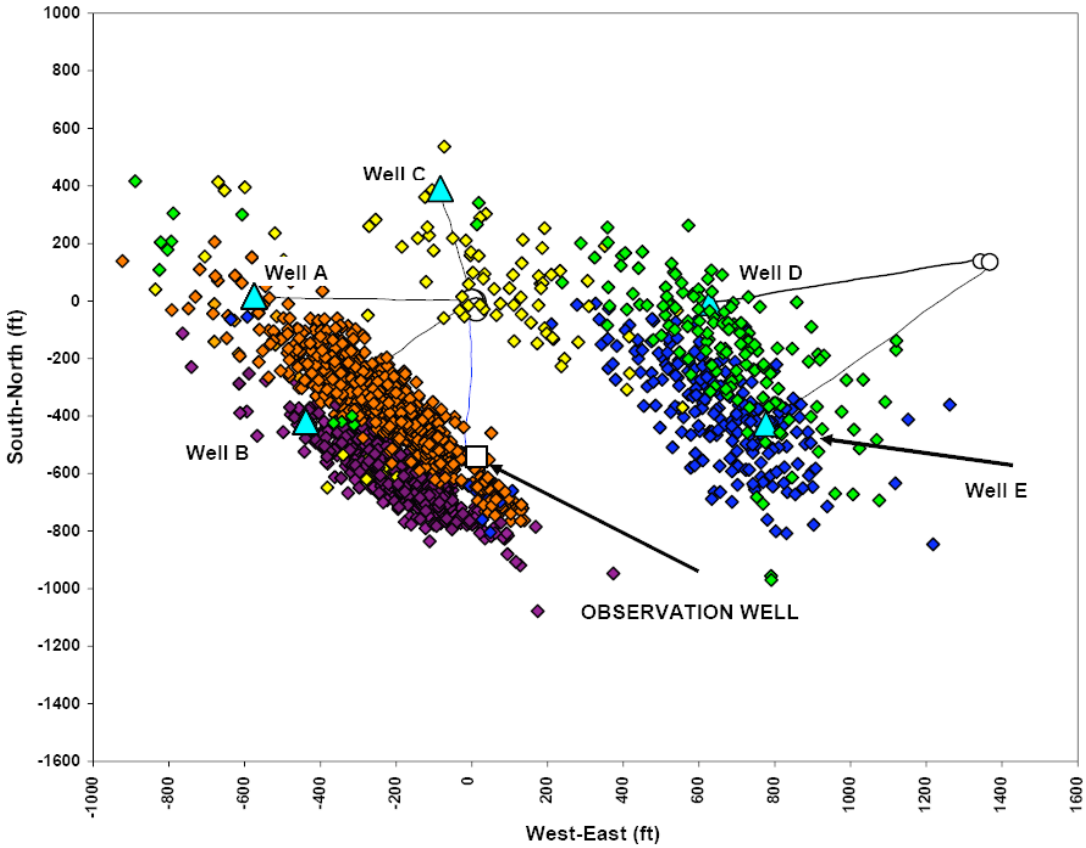

Figure 24. The event locations for all five wells. The events for all twelve fracture stages of Well A are shown with orange dots. The events for the nine fracture stages for Well B are shown with purple dots. The axes show the distances relative to the wellhead for Wells A, B and C. The cyan triangles show the bottom hole locations of each well. The monitor (observation) well is shown by the white box.

VIII. Velocity functions for migration traveltime table generation

The most obvious choice for imaging seismic data of all types is to use some variation of a migration algorithm. The time-lapse data from this survey can be migrated with any prestack migration algorithm adapted to the VSP geometry. We performed tests using a Kirchhoff prestack migration algorithm using a single velocity function of the form V = V0 + k*Z, where V is the velocity in m/s, V0 is a constant in m/s, Z is depth in m, and k is a linear gradient.

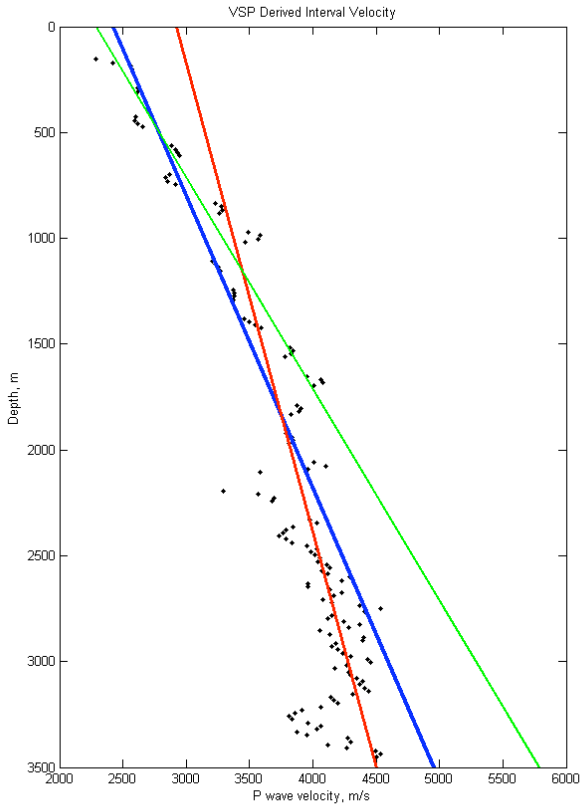

Figure 25. Interval velocities derived from a single VSP (courtesy Pinnacle Technology) shown in the black dots. The green line (V = 2286 + Z) fits the shallower portion of the well, the red line (V = 2921 + 0.4512 * Z) fits the deeper portion of the well, and the blue line (V = 2423 + 0.724 * Z) is a compromise to fit a larger portion of the well. Where V is velocity in m/s and Z is depth in m.

The analytic solution to the travel times between two points, q and p, in a linear gradient medium is given by:

$$T(q,p) = \left| \frac{1}{k} ar\cosh(1 + k^2 r^2 / (2V(q)V(p))) \right| \quad (1)$$

where r is the distance between the points p and q, and V(q) and V(p) are the velocities at the points q and p. This makes generating the travel time tables for the migration operation very simple, since only a single table is needed and it is analytically derived.

If there is no known regional velocity function, then the VSP geometry typically requires some additional velocity information from the surface down to the depth of the first receivers. Figure 25 shows the interval velocities derived from a single VSP in the area, which has receivers starting at 155 m depth. Three lines are plotted indicating visual fits of linear gradient velocity functions. The green line seems to fit the shallow portion of the well and has the form: V = 2286 + Z. The red line appears to fit the lower portion of

the well while honoring parts of the shallow section and has the form: V = 2921 + 0.4512 * Z. The blue line is a compromise between these fits which attempts to honor a larger depth range by under estimating the shallow zone and over estimating the deeper zone, using the form: V = 2423 + 0.724 * Z. The key to selecting the correct velocity function is to honor the travel times, so in fact the velocity function should be created from a fit to the slownesses, which does a better job of preserving the depth of the final image.

For the receiver travel times we used the "red" velocity function which attempts to honor the general velocity trend in the deeper part of the section which is given by: V = 2921 + 0.4512 * Z. Of course the issue with a single velocity function is that it does not honor the true travel times through medium and will create a problem matching depths at the well. Since we are looking to create an image of the fracture planes that is very accurately located in depth and space, the single velocity function will not perform well enough.

The image registration and depthing problem introduced by migrating with a single simple velocity function for both the shot and receiver tables complicates the task of identifying the fracture properties. To improve the image quality and reduce the location uncertainty, it is possible to use travel time tables derived directly from the 3D VSPs. In a similar manner, Brandsberg-Dahl et al. (2007) used VSP derived travel time tables for migrating surface seismic data. Representative arrival times of the first breaks were manually picked on about 200 of the "before" survey VSPs. Then these times were sorted into four groups, as shown in Figure 26b, corresponding to NE, NW, SW, and SE quadrants around the monitor well (Figure 26a).

Each of the four sets of picked travel times were interpolated to fill out complete travel times, providing master tables for travel times between the surface and all depth locations. Figure 27 shows the resulting four master travel time tables. Having four tables attempts to preserve any potential anisotropy in the velocity field. These four travel time tables provide the one way travel time from the surface shot and each potential fracture scattering point in the subsurface. In other words, these are the shot travel time tables.

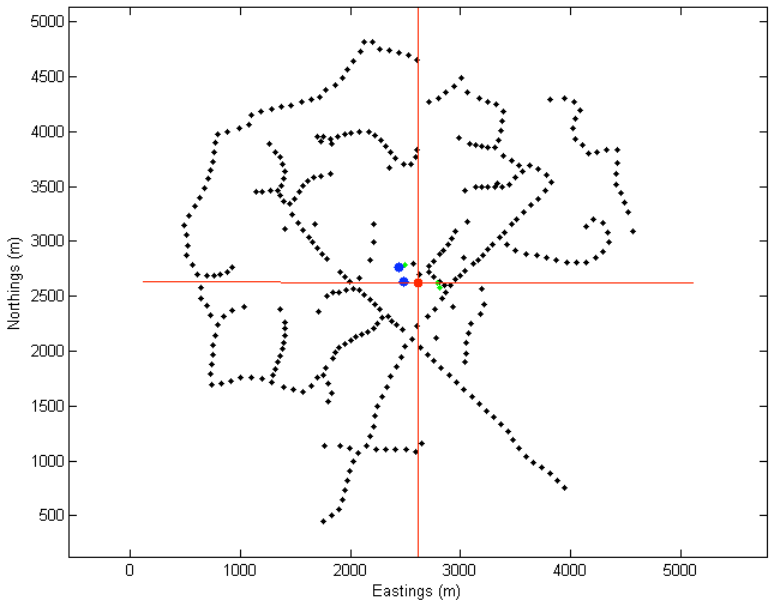

Figure 26a. Map of test area in Jonah Field divided into four quadrants. The red dot shows the location of the monitor well which recorded the time lapse VSPs and the microseismic events. The two blue dots show the bottom hole locations for the two hydraulically fractured wells studied in this paper. The black dots show the locations of the 338 surface seismic sources used for the time lapse VSP survey.

We can make an additional adjustment to the receiver travel time tables. Instead of using the linear velocity gradient model, the moveouts from the picked arrival times of the microseismic events give the exact travel times from the fracture plane to the monitor well. Unfortunately, when the microseismic events are recorded, only one tool depth level is recorded. For this survey that means that there are 11 to 12 arrival time picks for the well. This is not a very complete coverage of the 140 depth levels of the VSP, but it gives us an indication of the moveouts required. As we saw in the perforation tests, a constant velocity of 5182 m/s seems to make a reasonable fit of the arrivals across the array. The perforation velocities (Figure 23a) are more than 10% faster than the VSP velocities (Figure 25). This is consistent with observations for the Jonah Field by Maxwell et al. (2006).

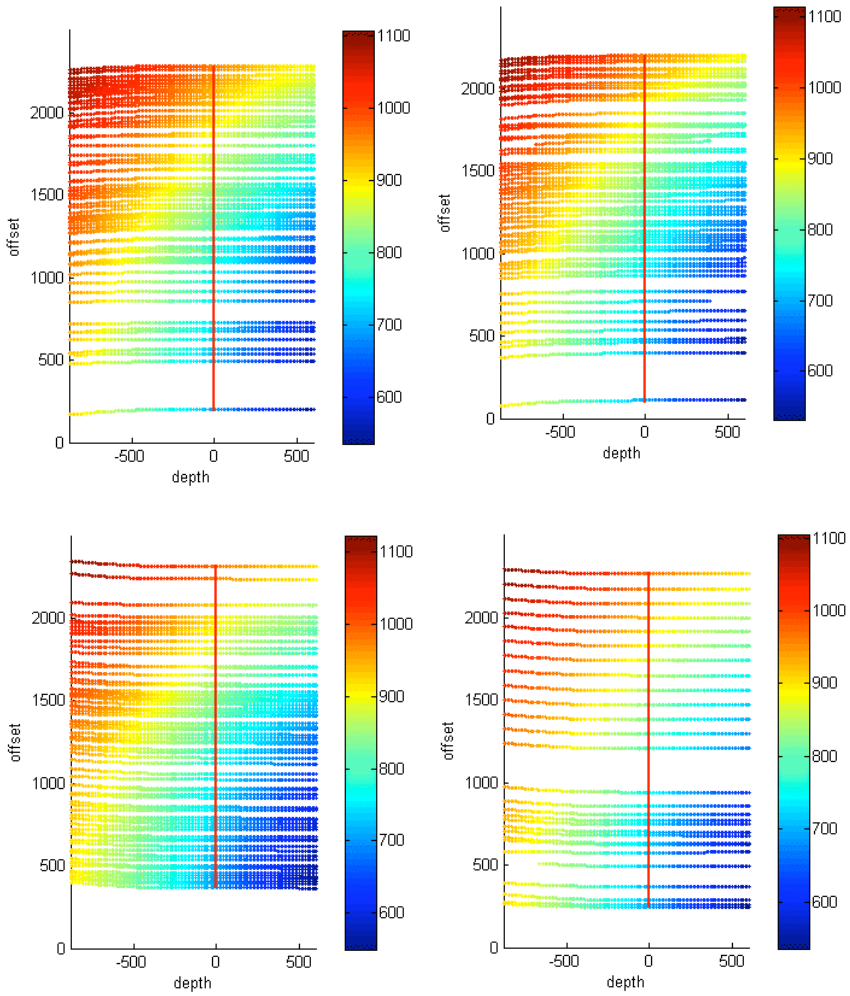

Figure 26b. Picked first break arrival times on 200 VSP records plotted by offset and depth and sorted into the NW (top left), NE (top right), SW (bottom left) and SE (bottom right) quadrants. The color shows the arrival times in ms. Note the depth scale is actually elevation relative to mean sea level.

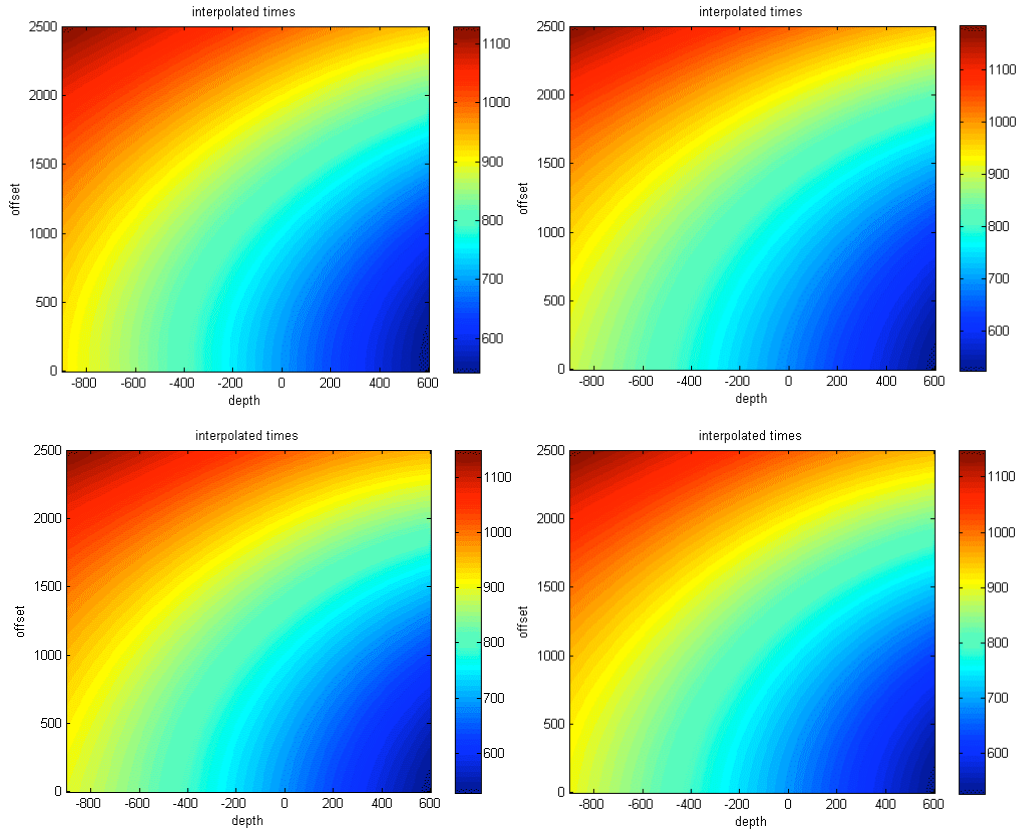

Figure 27. Interpolated first break arrival times created from the sparsely picked values in Figure 26, plotted by offset and depth and sorted into the NW (top left), NE (top right), SW (bottom left) and SE (bottom right) quadrants. The color shows the arrival times in ms. Note the depth scale is actually elevation relative to mean sea level.

IX. Migration imaging

We used the time lapse differences from source deconvolved data, and omitted those shot records for which we could detect problems in the data. For the migration we used the four shot travel time tables (from section VII) and the simple linear velocity function V = 2921 + 0.4512 * Z for the receiver travel time tables. Figure 28 shows three panels of migrated results through Well A. Panel (a) shows the result of migrating the before data with a mute on the direct arrival. Panel (b) shows the result of migration the after data, and Panel (c) shows the result of migrating the difference data. Since the goal is to fracture the sand units, as expected, the microseismic events track along formation units that we see in the before and after images. The projection to the surface (or track) of the image plane is shown in Figure 29 by the black line on the map.

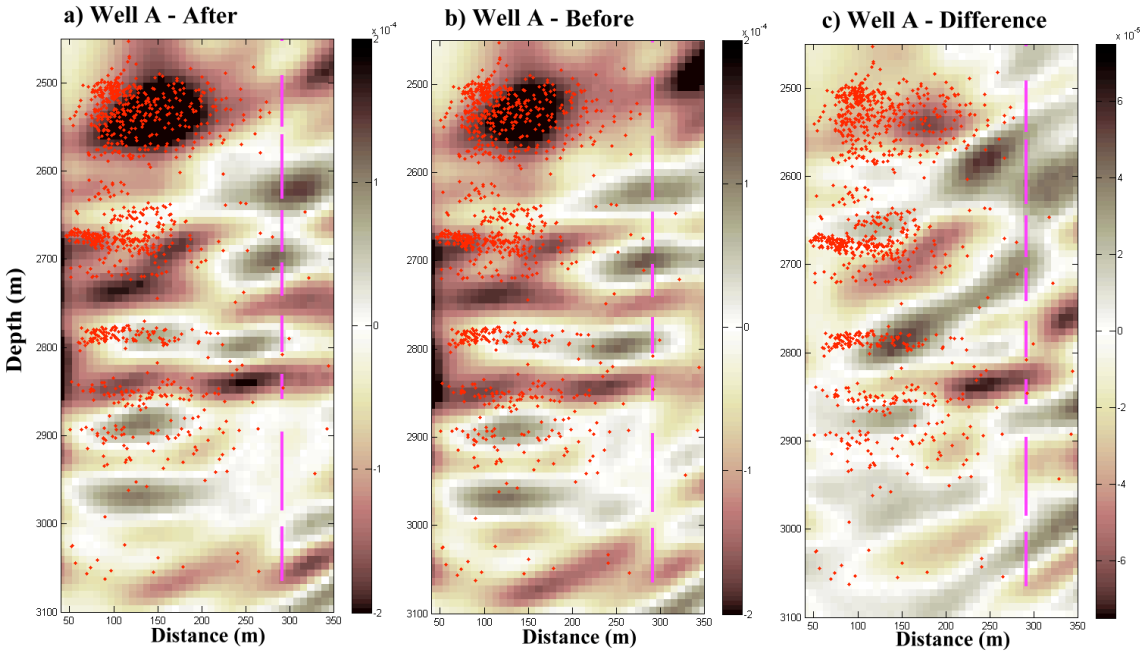

Figure 28. Migrated images through Well A using VSP picked times for the shot travel time tables and V = 2921 + 0.4512 * Z for the receiver travel time tables. a) Image created using the "after" fracturing data. b) Image created using the "before" fracturing data. c) Image created using the optimized difference between the after and before fracture data. The microseismic events from each well are plotted as red dots. The vertical pink lines denote the well track locations of the hydraulic fracturing injection points. The view is looking towards the south west so that the left side of each image is toward the South East and the right side is toward the North West. The gain is the same for panels a and b. Panel c is gained up about a factor of three as can be seen from the color bars.

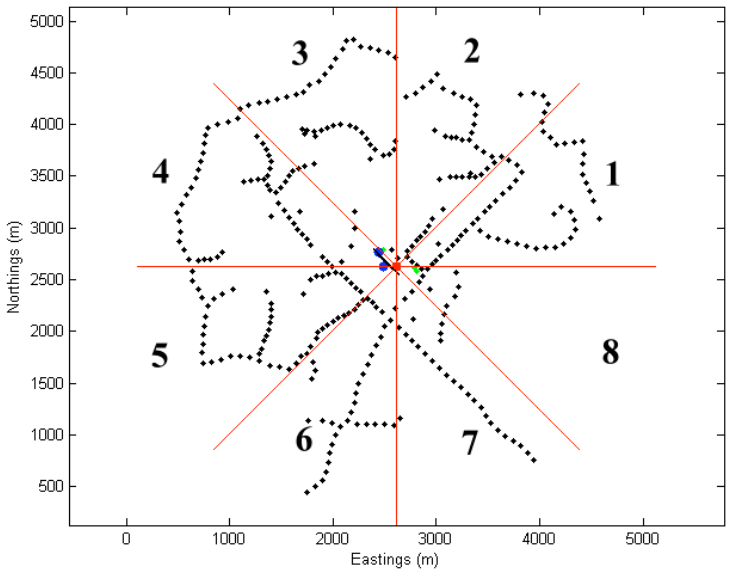

Figure 29. The location of the image in Figure 28 is shown by the black line through Well A. The red lines define the octants around the monitor well. The black dots are the locations of the shot points, the red dot is the monitor well, and the blue dots are the study wells A and B.

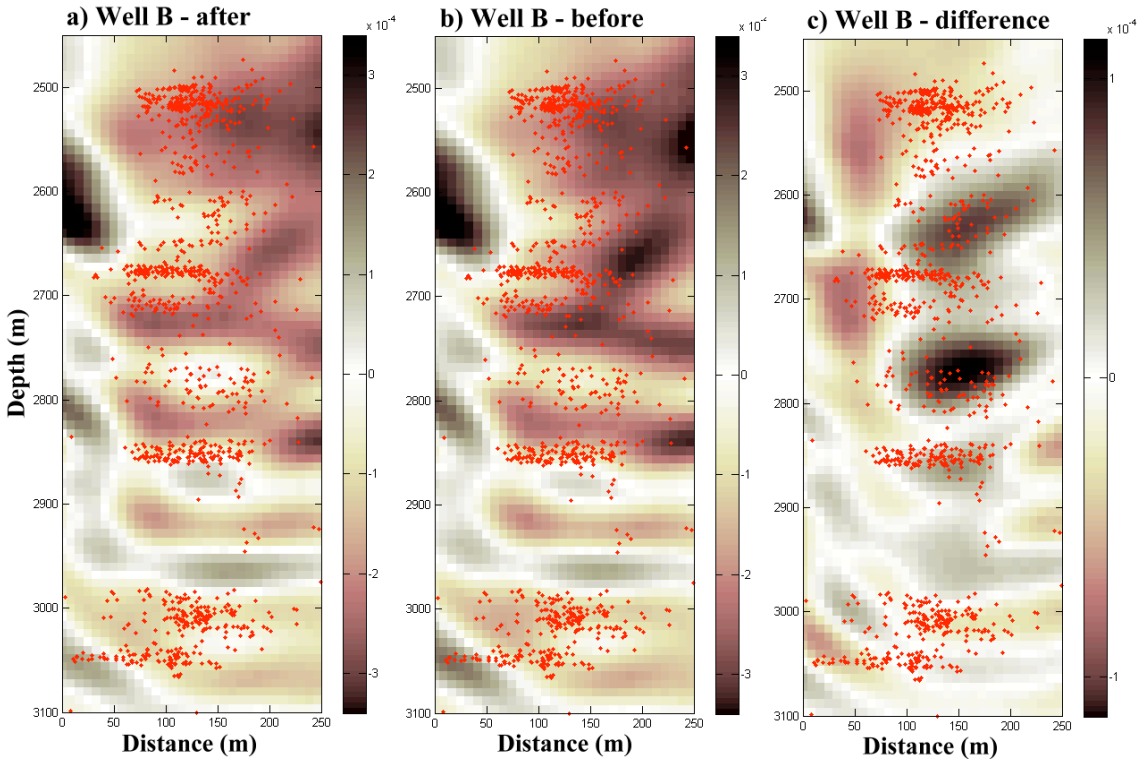

Figure 30. Migrated images through Well B using VSP picked times for the shot travel time tables and V = 2921 + 0.4512 * Z for the receiver travel time tables. The well track is a vertical line at about 200 m on the distance scale. a) Image created using the "after" fracturing data. b) Image created using the "before" fracturing data. c) Image created using the optimized difference between the after and before fracture data. The microseismic events from each well are plotted as red dots. The view is looking towards the South West so that the left side of each image is toward the South East and the right side is toward the North West. The gain is the same for panels a and b. Panel c is gained up a factor of three as can be seen from the color bars.

To test the sensitivity to the velocity between the fracture and the monitor well, we ran a range of constant velocities for the receiver travel time tables. Figure 32 shows our reference velocity model from Figure 28a and three velocities of 5182, 5486, and 5791 m/s. The migrations using the constant velocity receiver table have a different character from the linear gradient migration. They are more similar in content and seem to show large amplitudes near the well bore in the deeper section.

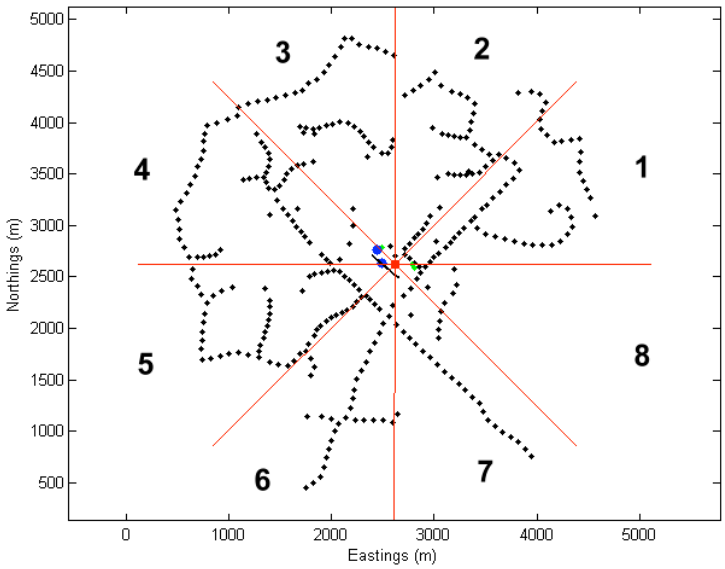

Figure 31. The location of the image in Figure 30 is shown by the black line through Well A. The red lines define the octants around the monitor well. The black dots are the locations of the shot points, the red dot is the monitor well, and the blue dots are the study wells A and B.

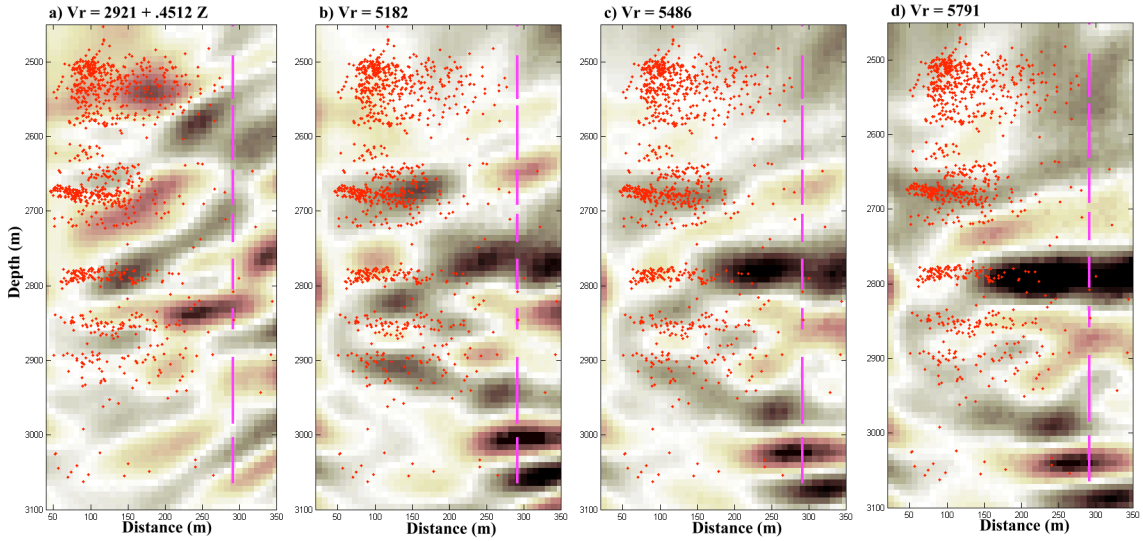

Figure 32. Migrated images of the time lapse data through Well A using VSP picked times for the shot travel time tables and four different velocity functions for the receiver travel time tables for the receiver travel time tables. a) Receiver velocity of V = 2921 + 0.4512 * Z. b) Receiver velocity of V = 5182 m/s. c) Receiver velocity of V = 5486 m/s. d) Receiver velocity of V = 5791 m/s.

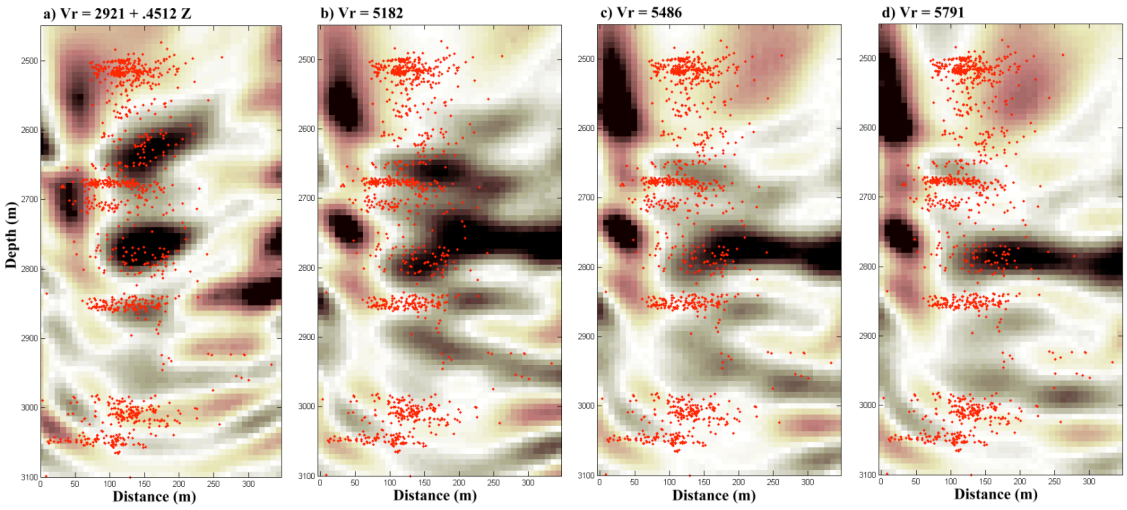

Figure 33. Migrated images of the time-lapse data through Well B using VSP picked times for the shot travel time tables and four different velocity functions for the receiver travel time tables for the receiver travel time tables. The well track is a vertical line at about 200m on the distance scale. a) Receiver velocity of V = 2921 + 0.4512 * Z. b) Receiver velocity of V = 5182 m/s. c) Receiver velocity of V = 5486 m/s. d) Receiver velocity of V = 5791 m/s.

X. Azimuthal images

We might expect that the strength of the reflected and/or scattered energy from the fractures will be different from the background lithology. To test this idea, we extract images using only shots in individual octants as shown in Figures 29 and 31. From our model studies above, we found that the best images of the fractures will be obtained from shots aligned in a circle or arc around the monitor well. Those geometries like columns 1-3 and 7 and 8 in Figure 15 produced the best fracture images. Thus we expect that the shots in octants 6, 7, and 8 in Figures 29 and 31 of the Jonah acquisition map will not contribute constructively to an image of the fractures, therefore we omit these octants from the displays.

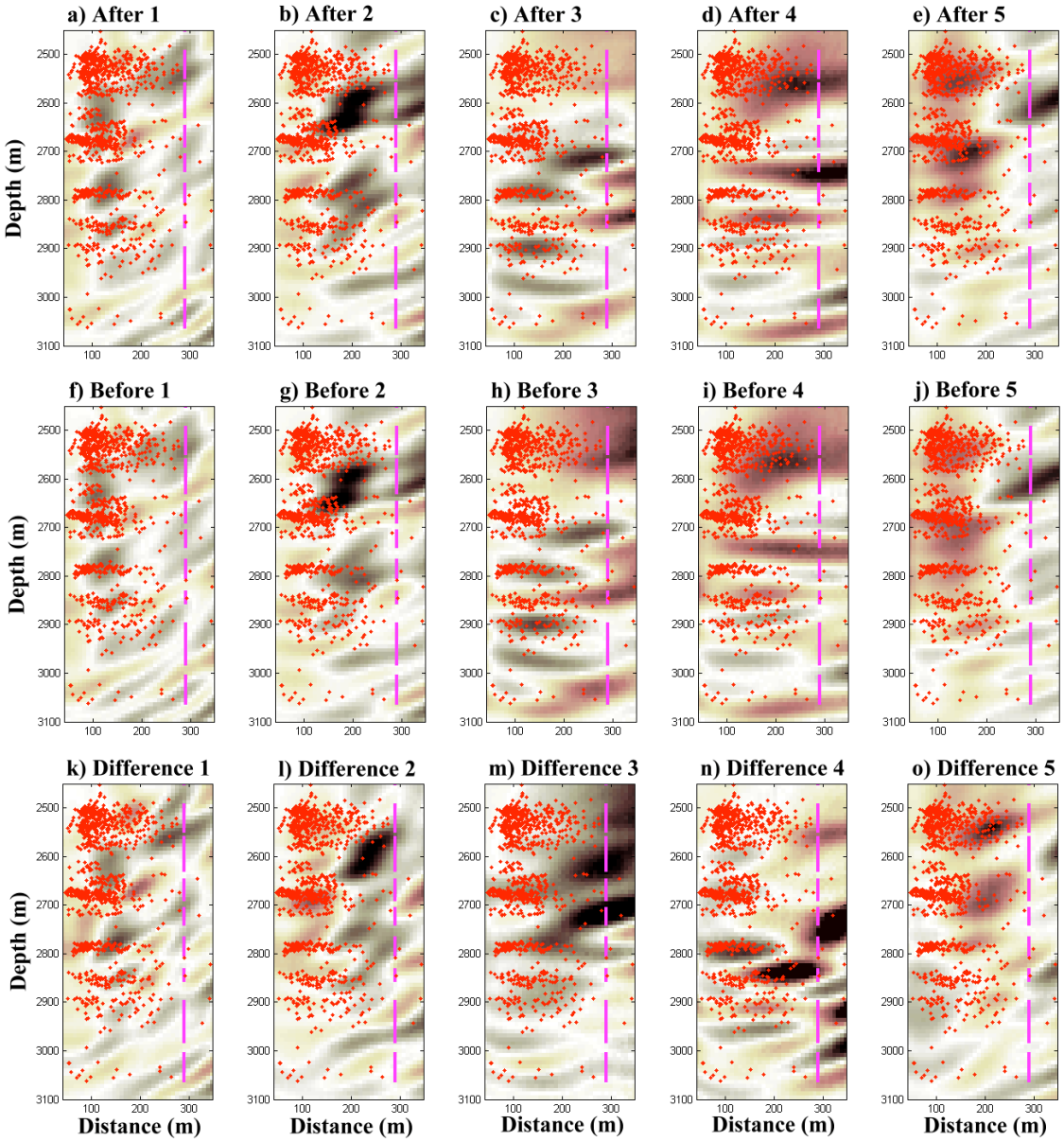

Figure 34. Migrated images through Well A using four VSP derived shot tables and receiver tables generated from V = 2921 + 0.4512 * Z. Each octant panel is created using only those shots that fall in its corresponding octant in Figure 29. Each "after" and "before" panel is plotted with the same gain relative to each other. The "difference" panels are gained a factor of 3 times the "after" and "before" panels. The microseismic events from each well are plotted as red dots. The vertical pink lines denote the well track locations of the hydraulic fracturing injection points.

We first separate the migrated images through Well A in Figure 28 into the contributions from the first five octants. Figure 34 shows the separate octant contributions to the "after" survey in the top row, the "before" survey in the middle row, and the "difference" or time lapse survey in the bottom row. We see that the after and before surveys are very similar. While the difference images have some similarities to the before and after survey, there are many features which are distinctly different from the other two images. Figure 35 shows the same analysis of for the line through Well B.

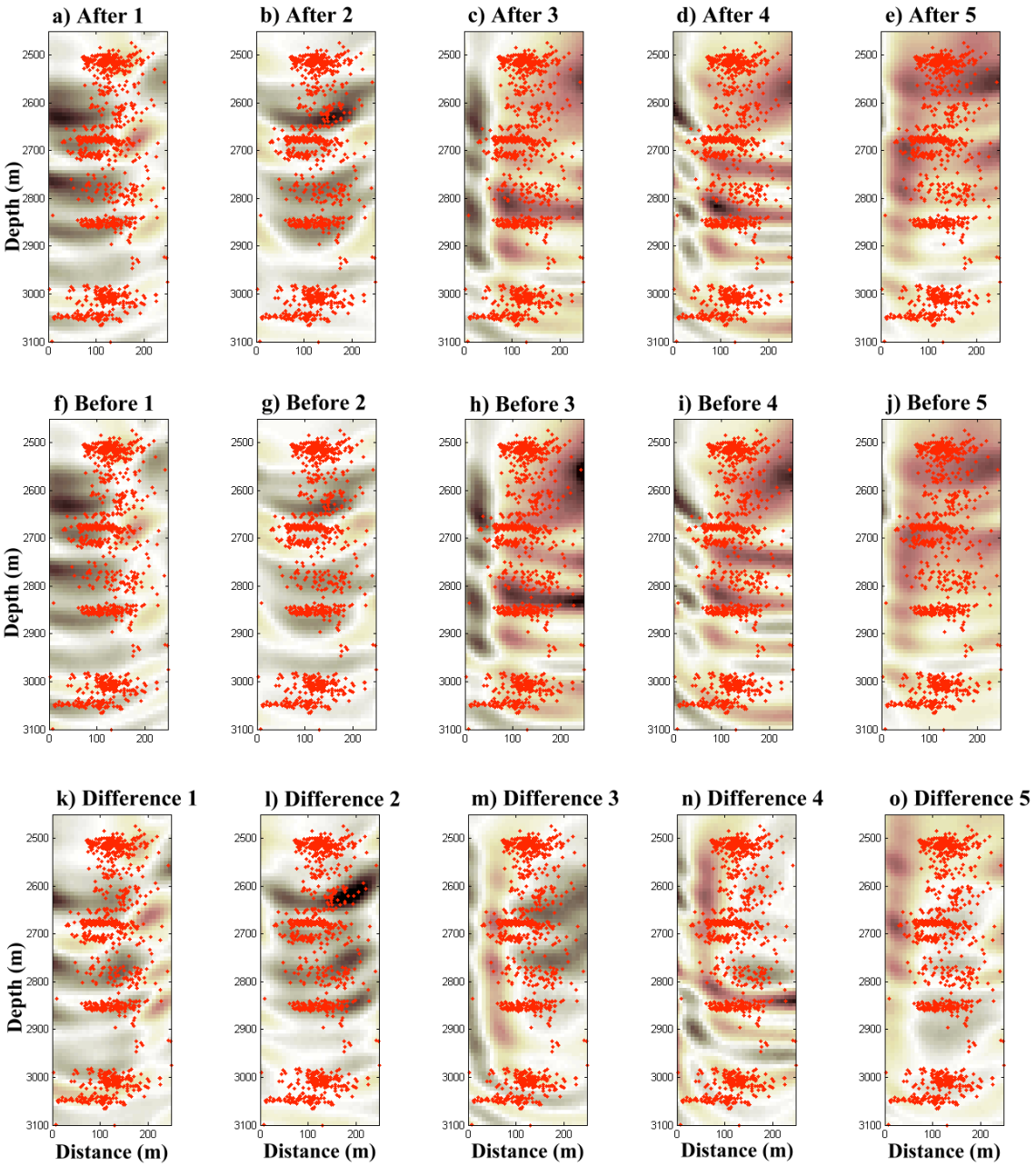

Figure 35. Migrated images through Well B using four VSP derived shot tables and receiver tables generated from V = 2921 + 0.4512 * Z. Each octant panel is created using only those shots that fall in its corresponding octant in Figure 31. Each "after" and "before" panel is plotted with the same gain relative to each other. The "difference" panels are gained a factor of 3 times the "after" and "before" panels. The microseismic events from each well are plotted as red dots.

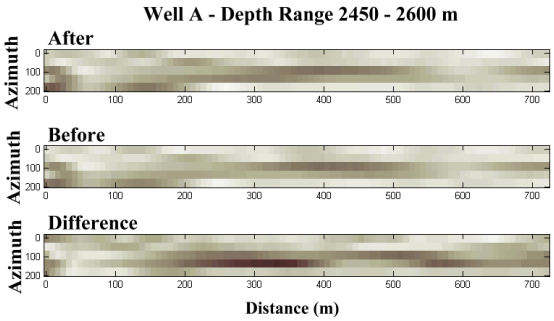

Figure 36a. Power in the azimuthal images through Well A in the first depth range. The vertical axis is azimuth in degrees. The horizontal axis is distance.

.

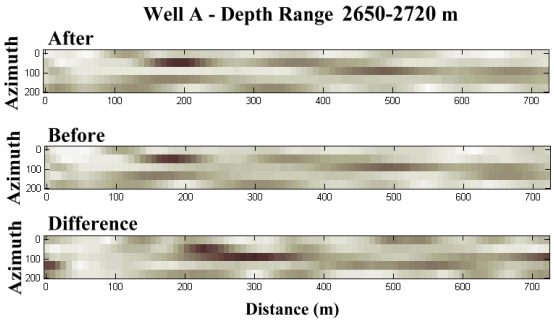

Figure 36b. Power in the azimuthal images through Well A in the second depth range. The vertical axis is azimuth in degrees. The horizontal axis is distance.

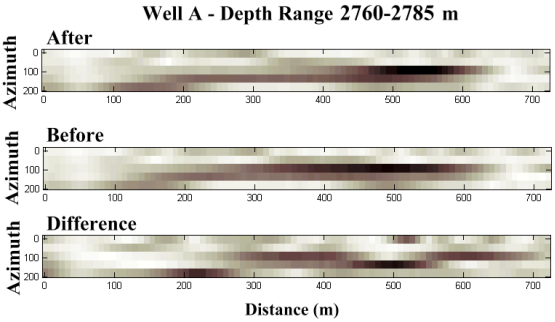

Figure 36c. Power in the azimuthal images through Well A in the third depth range. The vertical axis is azimuth in degrees. The horizontal axis is distance.

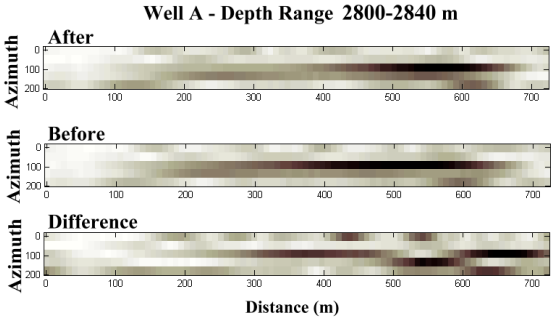

Figure 36d. Power in the azimuthal images through Well A in the fourth depth range. The vertical axis is azimuth in degrees. The horizontal axis is distance.

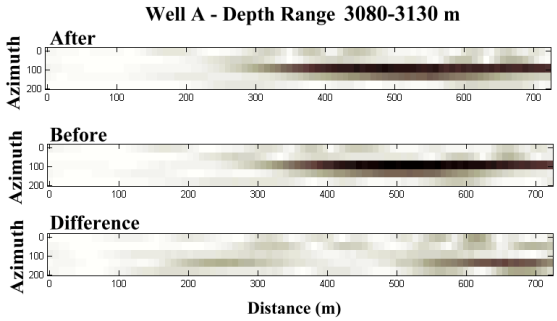

Figure 36e. Power in the azimuthal images through Well A in the fifth depth range. The vertical axis is azimuth in degrees. The horizontal axis is distance.

Next, we further analyze the azimuthal differences in scattering amplitudes. For the image through Well A, we compute the energy in each azimuth image in Figure 34 over 5 depth ranges: a) 2450-2600 m, b) 2650-2720 m, c) 2760-2785 m, d) 2800-2840 m, and e) 3080-3130 m. We compute the RMS energy in each trace (horizontally) in each of these depth ranges for each azimuth. Each part of Figure 36 shows the results in three panels of the after survey (top), before survey (before), and difference survey (bottom). The vertical axis in the part is the octant given in degrees from counterclockwise from East. The horizontal axis is the distance along the fracture plane. So Figure 36a gives the azimuthal energy along the fracture plane over the depth interval from 2450 to 2600 m. So we see that the before and after-fracturing surveys have virtually the same reflectivity as a function of azimuth. We also see that the difference image is significantly different. This observation holds for all of the depth ranges.

XI. Discussion

Our model studies have demonstrated that scattered energy off a fracture plane can be captured and imaged using a time-lapse VSP acquisition geometry. Open, compliant fractures scatter more energy than closed, stiff fractures. We do not know how to parameterize the fracture compliance properties in an absolute sense. But we have used a range of compliances and have shown that changes in compliances can be detectable. The topic of modeling fractures is immature, active, and unresolved at this point in time. We have used a "simple" 3D elastic, anisotropic modeling method which, no doubt, will ultimately be replaced with more advanced methods over time.

In order to study the effects of acquisition geometry on the quality of the images produced, we used a constant velocity scattering model. Using the model of six vertical fractures along a horizontal well, we looked at eight different surface configurations of shots. In each case, arcs of surface shots produced the best quality images of the fractures. Three different types of scattering were modeled in the study: uniform, dipole, and quadrupole. Also tested were scattered P and S waves. These cases were, by design, extremely simple, kinematic, single scattering, constant velocity models. The point of the exercise was to test whether there is enough moveout discrimination, frequency bandwidth, and surface coverage to create good images of the fracture zones. We found

that arcs of surface sources performed much better than a line of sources. There are even preferred orientations of arcs with respect to the fractures and monitor well, if a full circle is impossible to implement.

Preprocessing of the time lapse VSP data turned out to be the biggest challenge. Initial work showed that simple filtering, bad trace editing, and a spectral ratio phase and amplitude matching seemed adequate. However, subsequent analysis showed that the arrival times for the microseismic events will likely be very close to the first breaks. Thus the spectral ratio method we had employed was unsuitable as it removed scattering close to the first arrivals. Ultimately, we implemented a source deconvolution methodology that estimated the source by aligning a stacking the first breaks. A source wavelet of 600 ms was used for each shot point and was removed from the data by spectral division. This process was damped by 1% white noise, which introduced some high frequency noise. This was later removed by band pass filtering. This process allowed differences close to the first breaks to remain in the time-lapse records. We believe that even better results might be possible if we had used a longer window for the source wavelet—for example, the entire trace. The entire downgoing wavefield will be reflected off the fracture so that using a longer source wavelet would allow the multiples to add into the signal of the scattered energy.

We formed the differences between the after and before records using an optimized differencing scheme. It used a sliding window down each trace to minimize the energy in the difference by determining an optimal scale factor to multiply each window of the before trace before subtraction. This worked very well. We also looked at allowing the sliding time window to shift slightly in time with respect to the after record. The idea was to find the best alignment between records before subtraction. This did not work, most likely due to the simplistic implementation we used. It is likely that a more robust implementation would yield better results.

We discovered that about 10% of the shot records contain visually obvious problems. It appears that for some depth levels the data got corrupted before it was received. It may be that the simultaneous vibrator trucks in the field were out of sync part of the time, or that records were erroneously added together that were not related. In these cases it was obvious that there were multiple "first arrivals". Typically these arrivals were about 200 ms early or late. It is not known what other problems there might be in the data that are not detectable by simple visual inspection.

The microseismic data and perforation shots were processed by Pinnacle Technology to extract arrival times, source locations, and velocities. We did not attempt to quality control these results. We used the tabular data provided to us. The microseismic arrival times revealed that the scattered energy will likely arrive very close to the first breaks on the VPS records, since the one-way times are all less than 100 ms. The analysis provided from the perforation shots showed that the velocities at the reservoir depth were significantly higher than the measured reference VSP interval velocities, which were nearly all less than 4500 m/s.

The first break arrival times were picked for over 200 surface shot locations. These picks were interpolated to provide the shot travel time tables for migration. The tables were sorted in quadrants around the monitor well, which provided four independently derived travel time tables, one for each quadrant. This allowed the preservation of any anisotropy in the field. A second pass of arrival time picking was performed later for the purpose of source deconvolution. In this case every shot record of the before survey was picked. These picks could be reinterpolated to give a set of more accurate travel time tables. This may improve the quality of imaging in future work.

Migrated images were created through the microseismic clouds for two wells, A and B. For reference, the "before" and "after" data sets were also imaged. As expected, since there should be only subtle changes between these surveys, the migrated images of the before and after cases look very much the same. Small changes are visible, however. Since the goal of the hydraulic fracturing was to crack the tight sands, the microseismic events have a tendency to follow the structural features of the before and after survey images.

The migrated time-lapse images show generally higher amplitudes near the treatment well and near the zones with higher numbers of microseismic events. Changing the migration velocity makes significant changes in the images. Thus it is very important to determine the appropriate velocities to tie the microseismic events to the time-lapse images. The best quality images for Well A appear to be from using constant velocities for the receiver tables from the microseismic data. Using the microseismic derived constant velocities for the receiver time tables (Figure 32) appears to create realistic bi-wing images in Well A with significant changes in "fracture quality" evident.

We study the azimuthal scattering of the fractures by creating separate images from the shots in 5 octants around the monitor well (see Figure 29). We omitted octants 6 and 7 because they tended to have linear, radial shot distributions, which our modeling showed to be detrimental to the image. We also omitted octant 8 because it only had eight very near offset shots. What we found is that the azimuthal scattering of the time lapse data is quite different than the azimuthal reflectivity from the "before" and "after" surveys. If the time-lapse data mimicked the "raw" surveys, we would suspect that it was just subtracted poorly. Since they are different, it is possible that they are independent from each other.

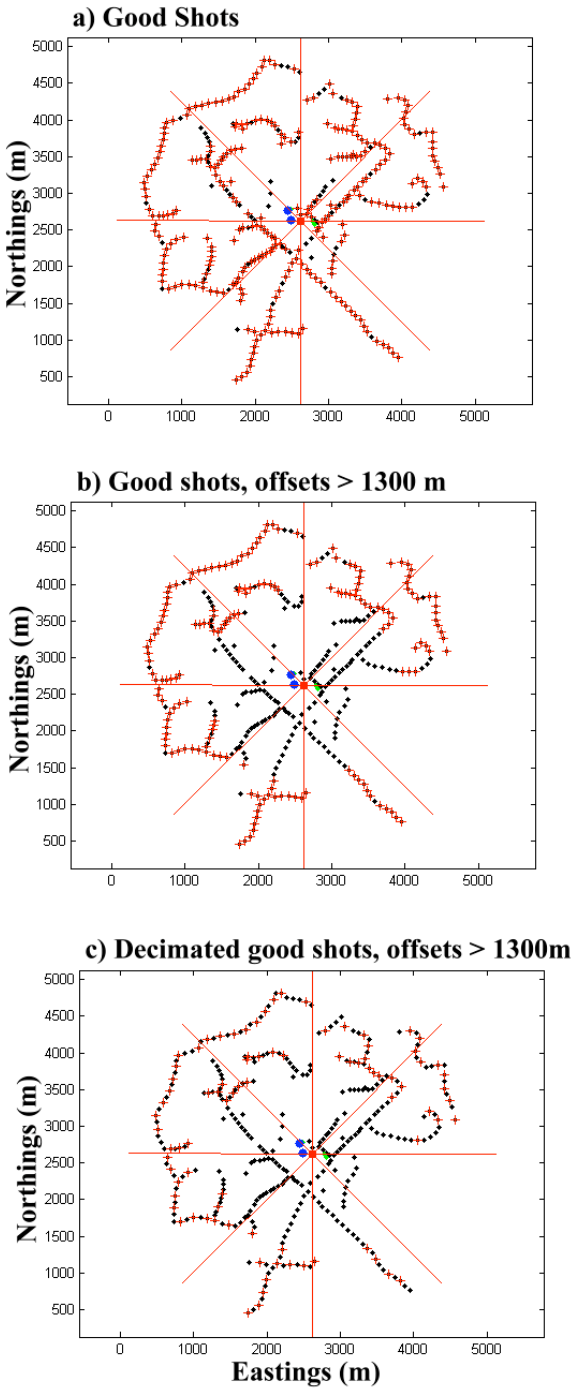

Figure 37. Survey map showing in red crosses the locations of a) all good shots, b) all good shots with offsets greater than 1300 m, and c) every other good shot with offsets greater than 1300 m. All other symbols are defined in the caption for Figure 16.

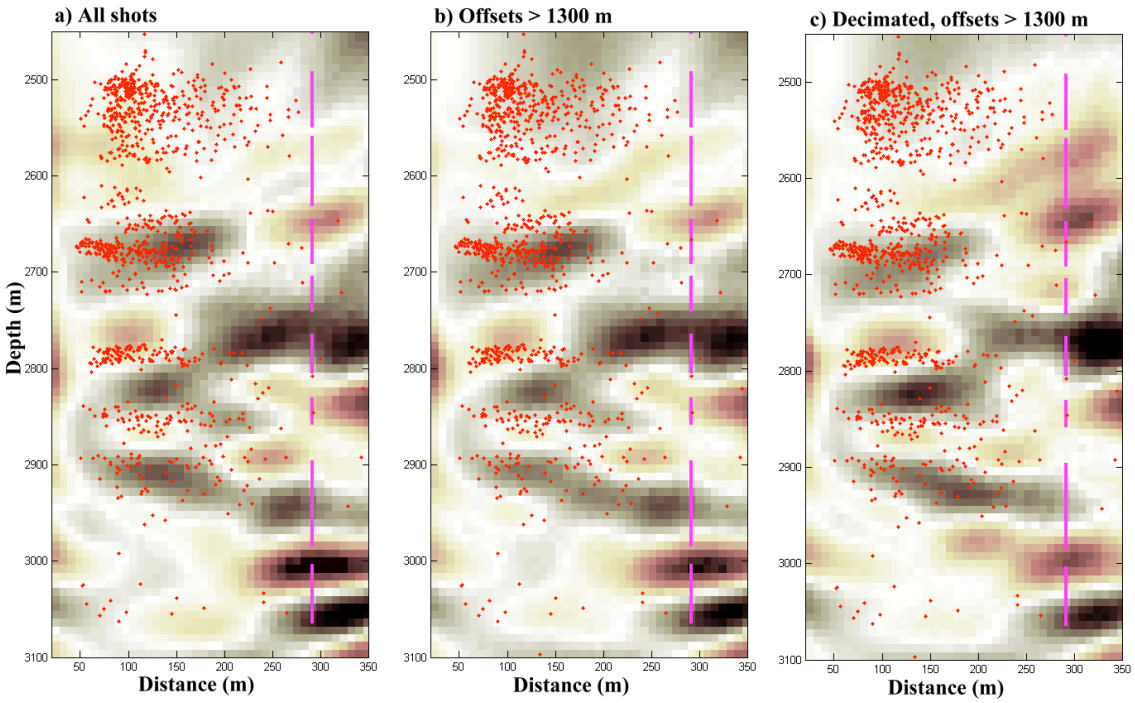

Figure 38. Migrated images using a) all good shots (shown in Figure 37a), b) all good shots with offsets greater than 1300 m (shown in Figure 37b), and c) every other good shot with offsets greater than 1300 m (shown in Figure 37c).

For future studies, it is important to be able to determine the acquisition requirements for obtaining these images. Figure 37 shows three different sets of shot locations used for creating the corresponding images in Figure 38. As before, in these images we omitted the shots from octants 6, 7 and 8. From these results it is clear that while there are some differences between these images, for the most part they are stable with respect to the offset range and the number of shots used. Therefore if required, it may be possible to acquire the next survey with reduced surface coverage, using shots larger than 1300 m from the monitor well and spaced farther apart.

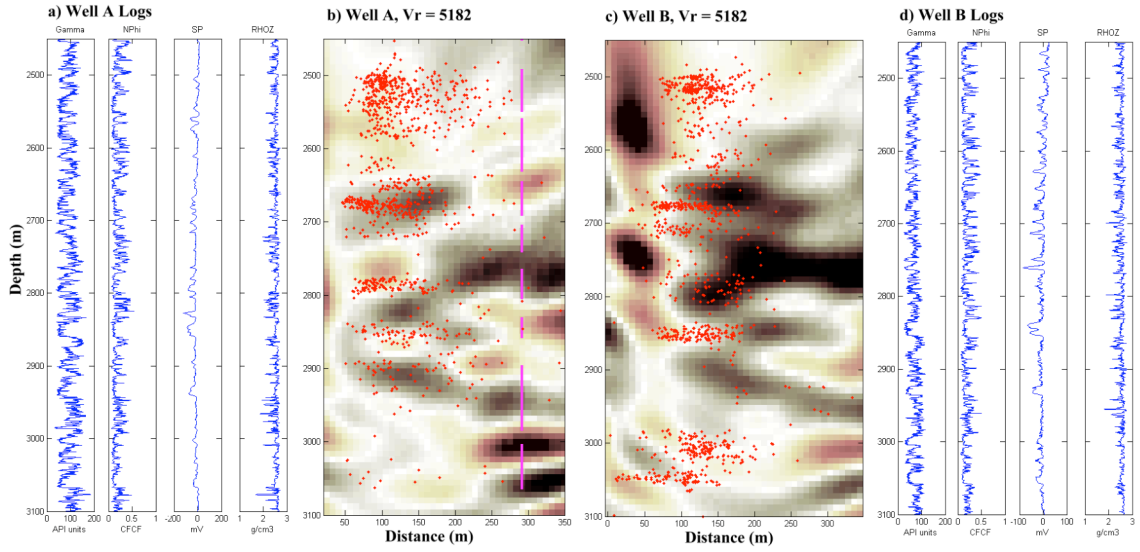

Figure 39. The well logs and final migrated images of the time lapse data through Wells A and B using VSP picked times for the shot travel time tables and a constant velocity of V = 5182 m/s for the receiver travel time tables. a) Logs for Well A. b) Migrated image through Well A. c) Migrated image through Well B. Note: Well B is located at distance of about 200 m on the image. d) Logs for Well B.

The well logs for Wells A and B were provided in LAS format version 1.2. We converted these logs to LAS format version 2 using the Canadian Well Logging Society's free tool on their website (www.cwls.org) and then extracted them into MATLAB using their read_las_file MATLAB script. Figure 39 shows the logs for both of these wells and the corresponding migrated images using a constant velocity of 5182 m/s for the receiver tables (from Figures 32b and 33b). This is the velocity, estimated from the perforation shots and used for locating the microseismic events, that gives better imaging results than the vertical velocity function. The logs show that this interval is an alternating sand/shale sequence. Generally it is possible to correlate the highly scattering zones in the migrated images with the sandy intervals that were fractured.

The left side of the migrated image through Well B (Figure 39c) shows two high amplitude events corresponding to a distance along the image from 0 to 50 m on the bottom scale. Since the plotting direction is shown viewed from the perspective of the NE to the SW, the left hand side of this image corresponds to the South East portion of the image plane shown in Figure 31. An examination of Figure 31 shows that most of the left hand side of the image is not illuminated adequately since we needed to omit the shots in octants 6 through 8. Thus it is likely that these high amplitude events may be just migration imaging artifacts, or in other words, edge effects. The right hand side of the image, corresponding to the North West, is located at nearly the same location as treatment Well A. Thus we see great similarity in the images on Figure 39b at distance of 300m and Figure 39c at a distance of 340m.

Comparing the two final images in Figure 39, we see that there is some significant scattered energy near the well bores and extending away from the wells into the surrounding formation, that is, from the right side of each image panel in Figures 39b and

39c and extending to the left. In Well A (Figure 39b), we see higher amplitude signals at depths of 2650-2700m, 2750-2820m, 2900-2950m, and 3000-3100m. The deepest zone is quite prominent, but does not extend very far from the well bore. The intermediate depth zone between 2650 and 2950m has significant scattering away from the borehole. Above 2600m it is hard to detect significant scattering. In Well B (Figure 39c), we see similar results, that is, higher amplitude scattering is seen at depths of 2650m, 2720-2800m, 2850-2950m, and 3000-3100m. Again, the increased amplitude signals in the deepest zone (3000-3100m) are only visible near the well bore (far right side of panel), while the other high amplitude zones (2650-2950m) extend farther into the formation. Like Well A, there is very little scattered wave energy visible above 2600m. Limited production data suggests that the zones of high scattering amplitude extending away from the well bore (i.e., roughly 2650-2900 in both wells) may correspond to higher production (and therefore higher quality) fracture zones. Another observation from these figures is that the number and spatial extent of microseismic events (red dots on the images in Figures 39b and 39c) does not always correspond to the high scattering amplitude regions (see, for example, the zones above 2600m). Future research and analysis should be focused on investigating the relationship between time-lapse images, microseismicity, and fracture production

XII. Conclusions

Modeling results of time lapse VSP energy scattered off vertical hydraulic fractures show that they mimic the moveout of microseismic events created during the fracturing treatment. Simple synthetic models show that VSP acquisition geometries which encircle the monitor well and encompass the vertical fractures provide a better chance of imaging the fracture plans than geometries with linear, walk away VSPs. A 3D VSP can provide data derived travel time tables for the shot portion of the VSP migration algorithm used to image the fracture plane. The proper migration velocity is critical to the success of aligning the microseismic events with the fracture planes. If an extensive 3D VSP is not available, then a carefully derived local velocity function is required. The microseismic events can provide the velocity and/or moveout functions for the receiver travel time tables of the migration algorithm. It was also found that the vertical VSP velocities were significantly slower than the measured perforation shots. Since the shot travel time tables measure essentially the horizontal travel paths through the subsurface, a good estimate of the reservoir level anisotropy must be incorporated in these tables.

Careful preprocessing of the before and after fracture treatment 3D VSP surveys is also critical to successfully imaging the fracture planes. Simple steps like band pass filtering and bad trace edit are first applied. But just as important, simple quality control inspection of the raw data revealed that about 10% of the VSPs were contaminated with an unknown source of frequently acausal events. These records were omitted from the imaging process. Proper source deconvolution was required since the source wavelet between the surveys was different and even the overall gain was different by a factor of over 1000. The prestack, time-lapse data volume was created from an optimized difference of the after-fracturing survey minus the before-fracturing survey.

Migrated images through the microseismic event clouds of two wells were created varying many parameters. First, the before and after-fracturing surveys were imaged separately and were found to be quite similar. Second, the time-lapse volume was imaged. These images were quite different from the before and after-fracturing survey images. The migration velocities of the shot tables and receiver tables were varied to see their effect. It was clear that an accurate velocity is required and that the first breaks from the 3D VSP would provide the best shot tables. The velocities estimated from the microseismic events provided what seem to be realistic fracture geometry images. Variations on these fracture plane images may reveal the changes in fracture quality. Three fracturing zones were observed in the final images: 1) the deepest zone showed good scattering within 50 m of the borehole, 2) the intermediate depth zone shows good and moderate scattering out to about 300m, and 3) the shallowest zone showed limited scattering. Limited production information indicates that the intermediate depth zone may be the most productive, suggesting that the deep zone has good fracturing, but only near the well bore; the intermediate zone has good quality fractures out to about 300m; and the shallower zone has poor quality fractures. More analysis of the images, microseismicity, and production data are needed to understand these relationships more fully.

XIII. Acknowledgements

Over the course of the four years we have worked on this topic, and we'd like to specifically thank several of the many people who have contributed. First, we thank Nancy House (EnCana Oil and Gas) for having the foresight to collect the field data and inviting us to work on this joint project with Pinnacle Technologies. Julie Shemeta (formerly Pinnacle Technologies now MEQ Geo Inc.) has consistently provided data, support and help throughout this project. Rongrong Lu (formerly at MIT/ERL, now at ExxonMobil) helped in prototyping the concepts of this work from the beginning by generating most of the synthetic 3D elastic finite difference models and performed the preliminary processing of them. Yang Zhang (MIT/ERL) provided additional help generating elastic models and examining the microseismic arrival locations. Sean Maxwell (formerly Pinnacle Technologies, now with Schlumberger) and Norm Warpinski (Pinnacle Technologies) have provided technical support through out this project. Pete Smith (EnCana Oil and Gas) provided technical support and encouragement. Ted Dohmen and Peter Hennings (ConocoPhillips) have provided encouragement, review and technical ideas. Arthur Cheng (Cambridge GeoSciences) has provided ideas for VSP and microseismic data processing. Scott Leaney (Schlumberger) made acquisition geometry suggestions. We used the Canadian Well Logging Society's LAS utilities to convert and read LAS files and custom written MATLAB scripts for processing the VSP and microseismic data. We want to thank EnCana Oil and Gas for releasing this data to us and allowing us to partner with them on this project.

XIV. References

Coates, R.T. and Schoenberg, M., 1995, Finite difference modeling of faults and fractures, Geophysics, v.60, p. 1514-1526.

DuBois, D.P., Wynne, P.J., Smagala, T.M., Johnson, J.L., Engler, K.D. and McBride, B.C., 2004, Geology of Jonah Field, Sublette County, Wyoming, in AAPG Studies in Geology #52, Rocky Mountain Association of Geologists 2004 Guidebook: Jonah Field Case Study of a Tight-Gas Fluvial Reservoir, AAPG.

Brandsberg-Dahl, S., Hornby, B., and Xiao, X., 2007, Migration of surface seismic data with VSP Green's functions, The Leading Edge, 26 (6), 778-780.

Maxwell, S., Shemeta, J. and House, N., 2006, Integrated anisotropic velocity modeling using perforation shots, passive seismic and VSP data, Expanded Abstracts CSEG Annual Meeting.

Saenger, E. H. and Bohlen, T., 2004, Finite-difference modeling of viscoelastic and anisotropic wave propagation using the rotated staggered grid, Geophysics, v.68, no.2, p. 583-591.

Willis, M. E., Burns, D. R., Lu, R., Toksoz, M. N., 2007, Fracture quality from integrating time lapse VSP and microseismic data, The Leading Edge.

Willis, M.E., Willis, K.M. and Burns, D.R., 2008, Hydraulic fracture quality using microseismic and time lapse 3-D VSP data to located scattered seismic energy: Jonah Field, WY, Rocky Mountain Area Geologist Annual 3D Symposium, meeting, Denver.

Zhang, Y., Campman, X., Grandi, S., Chi, S., Willis, M. E., Toksoz, M. N, Burns, D. R., 2006, F-K domain characteristics of the seismic response of a set of parallel discrete fractures, 76th SEG Annual Meeting Expanded Abstract.

National Energy Technology Laboratory

626 Cochrans Mill Road
P.O. Box 10940
Pittsburgh, PA 15236-0940

3610 Collins Ferry Road
P.O. Box 880
Morgantown, WV 26507-0880

One West Third Street, Suite 1400
Tulsa, OK 74103-3519

1450 Queen Avenue SW
Albany, OR 97321-2198

539 Duckering Bldg./UAF Campus
P.O. Box 750172
Fairbanks, AK 99775-0172

Visit the NETL website at:
www.netl.doe.gov

Customer Service:
1-800-553-7681